Chapter 5

INSTABILITY MECHANISM IDENTIFICATION: REDESIGNED EXPERIMENTAL SETUP

5.1 Background

The present chapter aims to build upon the work of McLeod *et al.* [1] and the previous two chapters to further investigate the dominant driving mechanism experimentally. While the comparisons between the experimental data and the theoretical predictions presented in the previous chapters showed improvements with the reanalysis, there were further areas for improvement which will be addressed here. In particular, larger ranges of $D = d_o/h_o$ and ΔT were investigated with a completely redesigned experimental apparatus. Building upon previous work, a strong focus was placed on early time wavelength measurements and accurate thermal control and measurement to provide the cleanest comparison between experimental data and the predictions of linear stability theory from each proposed model to date. Additionally, we will measure the growth rate and the characteristic wavelength simultaneously with a new analysis procedure to provide the most comprehensive comparison between theory and experiment performed to date.

Nanofilm instability experiments have historically proven to be challenging for a number of reasons. Primarily, these difficulties stem from the minute size scales involved. Defects as innocuous as a piece of dust must be stringently avoided because they can be an order of magnitude larger than the nanofilm's thickness and will destroy the parallelism of the heating and cooling plates. They also serve as nucleation sites for nonlinear growth that can swamp the incipient instability growth. Beyond magnifying the importance of defects, the limited vertical scale means that experimental measurements of the wavelength are based on nanometer scale deflections of the interface which can be technically challenging to identify. This poses strict requirements on the optical measuring techniques to have this level of sensitivity. Next, the temperature drop across the nanofilm/air bilayer cannot be measured directly because the presence of a thermocouple or other direct temperature measurement device would disturb the parallelism and temperature profile in the setup. Consequently, the value of ΔT must be inferred through temperature simulations of the setup. Finally, achieving vertical parallelism to

within 100 nm over a lateral distance of centimeters is a difficult process that is further complicated by the fact that the system undergoes rapid heating which can lead to differential thermal expansion between components. Experimental components were chosen for their high thermal conductivities, not for their thermal expansion coefficients, so differential expansion can be a problem when trying to achieve parallelism over large distances. Due to the small scales involved, minute differences in the coefficients of thermal expansion can cause large changes in the observed interference fringes. The experimental setup and procedures described in the following sections were specifically designed to address these challenges and improve upon the experimental designs of previous studies.

The initial studies of Chou *et al.* [2, 3] and Schäffer *et al.* [4–6, 15] suffered from three major experimental limitations. Most importantly, their systems could not be observed during the deformation process. As such, they were limited to making measurements of the feature wavelength after the protrusions had touched the top plate and solidified. This restriction poses a severe obstacle when comparing to the characteristic wavelength derived from linear stability because linear stability analysis is a perturbative technique in the amplitude of the film height disturbance. Once the protrusions touch the top plate there is no guarantee that the resulting wavelength will be the same as the one predicted by linear stability. Second, these groups were limited in their temperature control and measurement. In the case of Chou *et al.*, the temperature was assumed to be equal to that of the heating plate and no ΔT values were reported because the system was assumed to be isothermal and the driving force was hypothesized to be temperature independent. In the case of Schäffer *et al.*, they took ΔT to be the difference between the setpoints of their heater and chiller. As will be shown in more detail below, this is problematic because the nanofilm and air layers make up a minuscule portion of the total thickness and there can be significant temperature drops in other components of the system, even if those components have much larger thermal conductivities than those of air. Finally, both Chou *et al.* and Schäffer *et al.* identified the dominant instability wavelength by measuring the distance between peaks by hand which is suboptimal when trying to identify a global characteristic in something that doesn't have long range order. The experimental setup of McLeod *et al.* [1] improved upon each of these limitations and this was the experimental setup for the data shown in Ch. 3 and Ch. 4. First, they used *in situ* optical observations to measure the characteristic wavelength at early times to more accurately compare to linear stability predictions. Second, they used finite element simulations to calculate the temperature drop across each layer

of the system and extracted only the temperature drop across the nanofilm and air layers. Finally, they used Fourier analysis to extract the characteristic wavelength of the instability instead of measuring distances by hand which was a more robust measurement technique.

The experimental setup presented in this chapter improves further upon the work of McLeod *et al.* in each of these key areas. We have improved the *in situ* observations by using a larger viewing area to observe the growth of more peaks for improved statistics. Additionally, we switched from the white light illumination used by McLeod *et al.* to single wavelength illumination to more clearly highlight the instability growth at early stages. In terms of temperature control and measurement we have improved accuracy through the use of platinum resistance temperature detectors (RTDs) which have a higher resolution than the thermocouples used previously (0.1 °C vs. 1 °C, respectively [46, 47]). We also accessed a broader range of ΔT values by improving the thermal contact between layers in the new setup and using a higher power heating element. Finally, we have improved the wavelength extraction technique by using a new fitting function derived specifically for this physical system which allows us to measure the wavelength and growth rate simultaneously. This fitting function is a marked improvement over the Gaussian or Lorentzian fitting functions used previously. Overall, the improvements to all areas of the experimental setup have made us much more confident in the determination of the dominant instability mechanism.

The remainder of this chapter is divided into five major sections. First, we describe the details of the experimental setup in Sec. 5.2. Then the finite element simulations used to compute the temperature drop across the polymer/air bilayer are described in Sec. 5.3. Next, the analysis procedure used to extract the wavelength and growth rate for each experimental run is delineated in Sec. 5.4. Sec. 5.5 then details the comparison of the measured wavelengths and growth rates to the proposed models through the scaled quantities presented in Table 5.4. Finally, we discuss the experimental results and some of the biggest experimental challenges in Sec. 5.6. We conclude by emphasizing that the TC model is best supported by this experimental data.

5.2 Description of Experimental Setup

The redesigned experimental setup was inspired by the setup described in Ref. [1] and a diagram of the new experimental setup is exhibited in Fig. 5.1. The major

features of the setup are briefly described here and then a detailed account of the setup is presented below. The setup was divided into two halves to facilitate the loading and unloading of samples for different experimental runs. The bottom half ends at the nanofilm and the upper half starts with the SU-8 spacers attached to the sapphire window. The top half of the setup was stationary and consisted mainly of the large aluminum chiller and the camera attached to the microscope which was used to observe the instability *in situ*. The bottom half of the setup was mobile to allow loading of samples and was composed of several translation stages and the heater which provided the driving thermal flux through the system. Most of the instruments were digitally controlled and all the instruments that interfaced with the computer were controlled by a custom MATLAB GUI.

Starting from the bottom of the setup and moving upwards, a motorized XY translation stage (HT1111, Prior Scientific) supported the bottom half of the experimental setup and allowed for nanofilms to be inserted into the setup with its long travel range. Vertical displacement of the nanofilm was controlled by a manual z-axis dovetail translation stage (DS40-z, Thorlabs) attached to an adapter plate (MRP3-0.125, Newport) which was separated by 3.2 mm thick fiberglass insulation (9323K21, McMaster-Carr) and 127 micron thick polyimide film (500HN Kapton, DuPont). To help ensure parallelism between the sapphire window and the supporting silicon substrate, the adapter plate supported 4 springs (#235, Jones Spring Co.) around four 1/4-20 screws which attached to an identical adapter plate. The presence of the springs gave the heater holder and nanofilm extra degrees of freedom to tip and tilt so that it could more closely conform to the spacers on the sapphire window and achieve better parallelism. The upper adapter plate attached to the custom fabricated aluminum heater holder through four 6-32 screws. To prevent excessive thermal losses through the supporting structure, the adapter plate and heater holder were separated by 127 micron thick polyimide and 2 layers of 3.2 mm thick fiberglass insulation. Inside the heater holder was an alumina ceramic heater which provided the thermal flux in the system through Joule heating and is described in Sec. 5.2.1. Thermal paste (Heat-Away 638, Aremco Products, Inc.) was used to provide a strong thermal contact between the aluminum heater holder and the silicon wafer (50.8 mm diameter, <100> orientation, 10-20 Ω-cm, thickness 279 ± 25 microns, Silicon Materials, Inc.). The thermal paste completely filled a rectangular path inset into the heater holder and then created a layer above the top of the holder where the silicon wafer was positioned. The inset's outer boundary was a square 25.4 mm on a side and the inner boundary of the inset was a square 12.7 mm on a side.

The thickness of the inset was 0.508 mm and the entirety of the inset was filled with thermal paste for every experimental run. Prior to insertion into the setup, the silicon wafer was spin coated with a solid polymeric nanofilm and these preparation steps are detailed in Sec. 5.2.2. In direct physical contact with the nanofilm was the sapphire window with patterned spacers which was held to the custom aluminum chiller (305 mm x 101.6 mm x 25.4 mm) using a vacuum created below the micro cover glass coverslip (25 mm x 25 mm x 0.15 mm, VWR). The instability was observed through a hole in the aluminum chiller using a camera attached to a microscope. The details of the image capture process are detailed in Sec. 5.2.3. Additionally, the entire setup was encased in a cardboard box to isolate the system from any ambient air currents. The whole optical table on which the microscope sits was surrounded by optical curtains and within these curtains a horizontal laminar flow clean bench ran continuously (CAP303-33691, Clean Air Products). As a final precaution against introducing dust and external contamination onto the nanofilm, a surgical mask (59928, Kimberly-Clark) and hair net (5357T1, McMaster-Carr) were worn in addition to a lab coat (414004-368, VWR) and nitrile gloves (Microflex Xceed) during sample preparation and the experimental runs.

5.2.1 Experimental Temperature Control

The temperature drop across the nanofilm/air bilayer, ΔT, is a crucial parameter when comparing the three proposed instability models because it is a distinguishing parameter between the SC and AP/TC models. Additionally, it is the only parameter which can be digitally controlled in the experimental setup. As such, ΔT was controlled in several ways. First, the electrical power dissipated by the alumina ceramic heater through Joule heating provided the heat flux through the system and was controlled digitally. An alumina ceramic heater of dimensions 25 mm x 25 mm x 1.1 mm with a resistance of 5 to 6 Ω (Induceramic) was contained in the aluminum holder described above. The heater was driven by a 30 V, 5 A programmable DC power supply (2200-30-5, Keithley) controlled by a desktop computer (Precision T3500, Dell) through a GPIB to USB converter (488-USB2, ICS Electronics) in MATLAB 2013a [25]. The aluminum heater holder also contained a platinum resistance temperature detector (RTD) with outer diameter 2.5 mm (RTD-3-F3105-36-T, Omega) which was inserted concurrently with thermally conductive paste to ensure good thermal contact. The RTD was located in the center of the holder directly above the heater. The RTD was monitored in real time by a logger (PT-140A, Omega) which interfaced with the desktop computer. The current and voltage

Figure 5.1: Diagram of the redesigned experimental setup

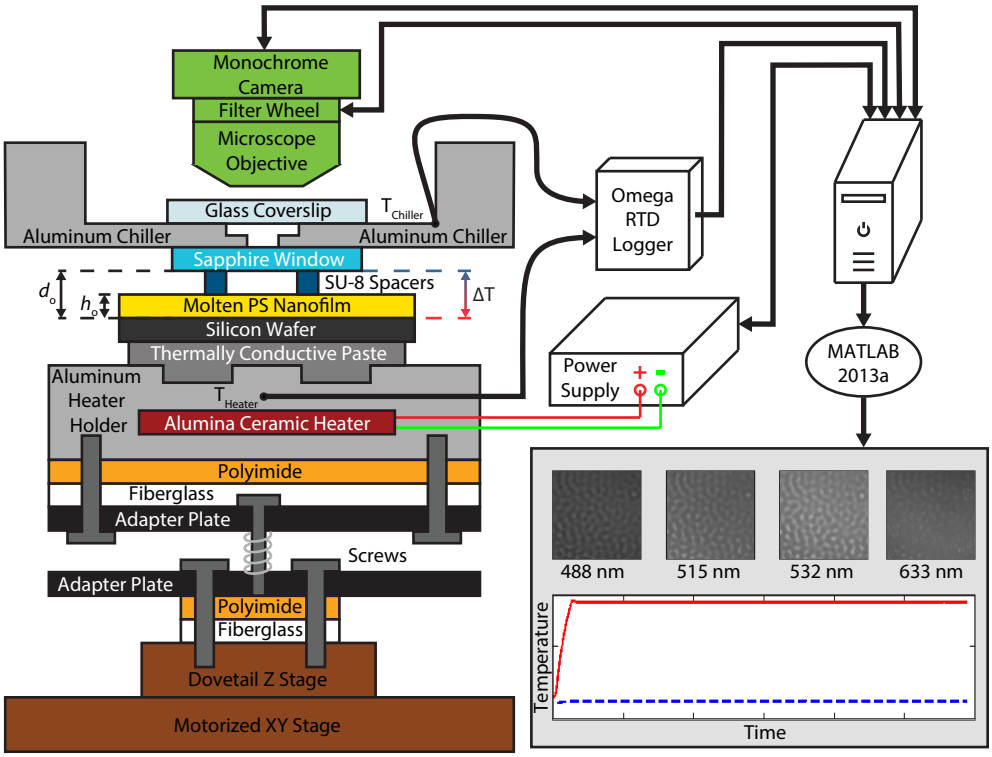

Diagram of the experimental setup (not drawn to scale) which was redesigned and improved from the one presented in Ch. 3 and Ch. 4. A full listing of the dimensions and materials can be found in the text.

of the power supply were controlled by the MATLAB GUI which implemented a PID loop evaluated approximately every half second with control parameters K_p = 0.1, K_i = 0, and K_d = 1 on the voltage. This PID loop was tuned by hand and we found that no integral gain was necessary to remove steady-state error, so K_i was set to zero. The feedback was implemented based on the temperature reported from the platinum RTD directly between the heater and the nanofilm and the temperature of this RTD was always found to be within 0.1 °C of the setpoint once the initial equilibration time (approximately 5 minutes) had elapsed. These parameters were chosen with an emphasis on minimizing overshoot of the temperature. The overshoot was less than 3 °C for any setpoint choice. The power supply imposed another restriction on the feedback loop because its maximum output voltage was 30 V and during initial heating this limit was often hit. For safety reasons, and to prevent large thermal shocks, we also restricted the maximum voltage increase to be less than 0.5 V in a single time step. Second, the external chiller which pumps water through the aluminum chiller had an active feedback loop which maintained

a fixed setpoint temperature of the external water bath. The aluminum chiller was attached to an external thermostat (RM6, Lauda Brinkmann) which pumped temperature controlled water through the chiller in a counterflow arrangement to expedite convective heat transfer. The temperature of the chiller was monitored with an RTD at the edge of the objective cutout and recorded by the same logger as the RTD in the aluminum heater holder. The advantage of using RTDs as compared to thermocouples in this system is that RTDs provide more precise measurements than thermocouples and the faster response time of a thermocouple was not needed. Finally, we enclosed the whole system in a cardboard box to prevent air currents from the laminar flow clean bench or the building ventilation system from interacting with our system. This prevented any external forced convection due to air currents and removed diurnal and seasonal variations in the steady state temperature profile.

5.2.2 Sample Preparation and Mask Fabrication

Prior to an experimental run, the polymeric nanofilm and mask patterns on the sapphire window were prepared. The polymeric nanofilms were created by spin coating a solution of the dissolved polymer onto a silicon wafer. During spin coating, the solvent evaporated, leaving a solid nanofilm ready for insertion into the experimental setup. The patterned spacers on the sapphire window were created photolithographically using standard techniques and these windows were reusable for many experimental runs.

The polystyrene (PS) (1.1k M_W, polydisperity 1.12, #771, CAS #9003-53-6, Scientific Polymer Products) was dissolved in reagent grade toluene (CAS #108-88-3) with weight percentages ranging from 1% to 8%. This solution was then filtered with an alumina matrix filter with 0.02 micron pore size (Anodisc 13, #6809-7003, unsupported filter, Whatman) in a stainless steel holder (#1980-001, GE Healthcare Life Sciences) attached to a 5 mL glass syringe with stainless steel Luer lock tip (5017, Cadence Science). Special care was taken to choose filtering components which did not dissolve in toluene, as previous attempts using polymeric filters and syringes showed unacceptable levels of defects due to contamination of the solution from dissolution of the filters and syringes. After initial filtration and storage in a glass jar with a PTFE lined cap (#12-100-276, Fisher Scientific), the solution was filtered again as it was dispensed for spin coating onto the silicon wafer. Spin speeds ranged from 1000 RPM to 3000 RPM with an acceleration of 1000 RPM/s (CEE-100, Brewer Science) for 30 seconds. The toluene evaporated during spin coating, so the PS nanofilm was ready for immediate thickness measurement with an ellip-

someter at a wavelength of 632.8 nm (Auto EL III, Rudolph). A single measurement was taken at the center of the wafer in the area which can be observed through the sapphire window to determine h_o. Previous ellipsometer measurements had shown that the thickness of a nanofilm spin coated with this instrument was consistent across the whole wafer to within the measurement uncertainty of the ellipsometer after the spin coater had been leveled. To level the spin coater, a spare 50.8 mm diameter silicon wafer was placed on the vacuum chuck. Isopropyl alcohol (IPA) was slowly dispensed in the center of the wafer and the direction of fastest spreading was noted. The wafer was spun until the IPA evaporated and the adjustable feet on the spin coater were adjusted to raise the direction of fastest spreading. This process continued until the IPA spread uniformly in all directions and reached the edge of the silicon wafer simultaneously. For more details on spin coating, please consult Appendix A.1.

When the nanofilm was inserted into the setup using the XY and Z translation stages, it was raised until it contacted the SU-8 spacers (SU-8 2000, Microchem) which were photolithographically patterned on the sapphire window (1 mm thick, 9.5 mm diameter, c-axis aligned, MSW037/040Z, Meller Optics). Using c-axis aligned windows minimized the birefringence of the sapphire window. Spacers were arranged in a hexagonal pattern at a radius of 3 mm and each individual spacer was circular with a 1 mm diameter. Before spinning the SU-8, the window was attached to a 25.4 mm square glass substrate (25.4 mm x 76.2 mm Gold Seal microscope slide scribed and broken to approximately 25 mm square, 3010-002, Thermo Scientific) with S1813 photoresist (Microposit S1813 G2 Photoresist, Dow). The sapphire/photoresist/substrate agglomerate was baked at 95 °C for 10 minutes on a hotplate (11301-016, VWR). By attaching the window to a substrate, the edge bead of the SU-8 was reduced and this allowed the spacers to be placed at a larger radius on the sapphire window while still preserving a uniform thickness. After baking the S1813, the SU-8 was spun onto the window using a spin coater (Model WS-400A-6NPP/Lite, Laurell) with speeds that varied between 1000 RPM and 3000 RPM and accelerations that varied between 1000 RPM/s and 3000 RPM/s for 60 seconds. After spinning, the SU-8 was pre-baked at 65 °C for 1 minute and 95 °C for 2 minutes. The window was then exposed to UV light through a custom patterned mask (UCLA Nanoelectronics Research Facility) for 60 seconds in a mask aligner (MJB3, Karl Suss). Then, the window was post-baked at 65 °C for 2 minute and 95 °C for 4 minutes. The SU-8 pattern was developed in SU-8 developer (MicroChem) for 30 seconds, followed by insertion into a bath of IPA

for 30 seconds. To detach the window from the substrate, the S1813 photoresist was dissolved with acetone and the window was rinsed with IPA to remove any residual acetone. The window was removed from the acetone as soon as it detached from the substrate (typically around 10 seconds) because long exposure of SU-8 to acetone before hard baking was found to crack the SU-8 and cause delamination from the sapphire. The developed window was then hard baked at 200 °C for 2 hours to complete the fabrication process. After the hard bake, the spacer heights were measured using a profilometer (XP-2, Ambios) and were ready for use in an experimental run. The spacer heights varied from 730 nm to 7 microns. After the experimental runs were completed, we observed that some PS remained underneath the spacers so the d_o values in Table 5.5 which represent the total gap thickness from the bottom of the nanofilm to the top of the air gap are equal to the initial film thickness plus the spacer height. For more details on mask fabrication, please consult Appendix A.3.

5.2.3 Optical Image Acquisition

Optical observation of the instability during deformation was accomplished through the use of a camera attached to a microscope. To accommodate the working distance (WD) of the microscope objective (10x EC Epiplan HD, WD = 14.3 mm, #422040-9960, Zeiss), a 50.8 mm x 50.8 mm x 19.1 mm section was removed from the center of the aluminum chiller. In the center of the cutout, a viewing hole (diameter 2.94 mm) allowed optical access to the film. This hole was designed to be as small as possible to maximize the possible temperature difference, but another hole (diameter 4.86 mm and depth 4.83 mm) was required for the light cone of the objective to be unimpeded. The microscope objective was attached to a Zeiss Axiotech 200 MAT microscope and the film was illuminated by a halogen white light bulb (HAL 100, Zeiss). The output of the microscope was filtered using narrow bandpass filters (FL 488-1, FL 514.5-1, FL 532-1, FL 632.8-1, Thorlabs) in a filter wheel (FW102C, Thorlabs) controlled by the desktop computer to aid with interferometric measurements of the film height. Since the light had been filtered to be effectively monochromatic, a grayscale camera (acA2500-14gm, Basler) was attached to the filter wheel to observe and record the film deformations dynamically on the computer. During the experimental runs, images were taken at time intervals of 15 seconds to allow time for the filter to rotate. This meant that a time series for each filter was taken with intervals between images of one minute.

5.3 Finite Element Simulations of Experimental Setup Temperature

With the set of thermal measurements and controls described above, the experimental ΔT was quite stable during the experimental runs. However, it was not possible to measure the temperature difference across the gap directly due to its small size (on the order of microns). Consequently, finite element simulations in COMSOL [28] were used to calculate the temperature of the experimental setup using the heat equation. Due to the vanishingly small product of the Prandtl and Reynolds number in nanofilm experiments [10], the temporal dependence of the heat equation can be ignored and we solved only Poisson's equation for the steady state temperature within each domain.

$$\boldsymbol{\nabla} \cdot (k_i \boldsymbol{\nabla} \mathrm{T}_i) = \dot{Q}_i, \tag{5.1}$$

where k_i is the thermal conductivity of the ith domain, T_i is the temperature, and $\dot{Q}_i$ is the contribution from any volumetric heat sources. Note that the symbol k has been used twice but it should be clear from the context whether thermal conductivity or wavevector is being indicated. In the absence of externally imposed boundary conditions both the temperature and thermal flux must be continuous at the interior interfaces between domains. If $\partial\Omega_{i,i+1}$ denotes the interface between the i and $i+1$ domains, then the simulations satisfy the following equations on $\partial\Omega_{i,i+1}$ for every i

$$\mathrm{T}_i = \mathrm{T}_{i+1}, \tag{5.2}$$

$$-k_i \boldsymbol{\nabla} \mathrm{T}_i = -k_{i+1} \boldsymbol{\nabla} \mathrm{T}_{i+1}. \tag{5.3}$$

Fig. 5.2(a) shows a diagram of the computational domain used for this study and the boundary conditions that were used. The layers are the same as Fig. 5.1, although we have not included layers below the alumina heater holder due to the large amount of thermal insulation nor the imaging components (the microscope objective, filter wheel, and camera) since they were not physically connected to any components which were actively heated or cooled. The thermal insulation beneath the aluminum heater holder was modeled by a thermally insulating boundary condition which is denoted by the black crosses in the figure. Note that the region between the glass coverslip and the sapphire window was continuously aspirated and so we assumed that there was no thermal conduction through this region. Therefore, the top of the sapphire, the inner portion of the aluminum chiller and the bottom of the glass coverslip were exterior boundaries which had a boundary condition of thermal insulation so that no flux passed normal to them. The simulation domain was chosen to be cylindrically symmetric. However, most of the experimental objects were

rectangular and so all rectangular objects were converted to cylinders with the same height. The radius of each cylinder was then chosen to preserve the total volume of the original experimental object. For a full listing of the simulation object sizes, see Table 5.1. The only domain which had volumetric heating (nonzero $\dot{Q}_i$) was the alumina ceramic heater and the value of the volumetric heating was set equal to the experimentally measured power supplied to the heater after the temperature setpoint was reached. The only other condition that was imposed on the interior of the domain was that the vertical wall of the chiller was set to be isothermal to the temperature measured experimentally by the RTD positioned there. In Fig. 5.2(a) this is denoted by the blue slanted lines. For the exterior boundaries, the vertical boundary at $r = 0$ had a no flux condition due to the cylindrical symmetry which is denoted by black crosses in Fig. 5.2(a). The bottom of the aluminum heater holder and the connected vertical edge directly beneath the edge of the holder also had a no flux condition. This was used because of the large amount of thermal insulation present beneath the holder. This insulation would be difficult to accurately model computationally and prevented most of the heat from traveling through the supporting materials, so it was assumed for this model that no thermal flux is lost to the plates supporting the heater holder. The remaining external boundaries represent the bounding cardboard box and were set equal to the ambient temperature of 23 °C.

At this point, we have a completely defined temperature simulation but have not incorporated the temperature measured by the RTD above the alumina ceramic heater which was used as the feedback setpoint. This additional value allowed us to calculate the thickness of the thermal paste layer which was not well characterized. The amount of thermal paste which provided thermal contact between the silicon wafer and the aluminum heater holder was not measured and varied somewhat between experimental runs. Additionally, the exact distribution could not be measured because the thermal paste shifted as the wafer and nanofilm were brought into contact with the SU-8 spacers on the sapphire window. The thermal paste also showed a change in viscosity as the temperature of the heater increased which led to further settling during the initial times before equilibrium. While we could not measure the thickness of this layer, we did quantify the lateral extent by measuring the residual thermal paste left on the silicon wafer after removal. Since there is only one unknown parameter left in the simulation (the thermal paste thickness) and we have one more experimentally measured value (T_{heater}), we varied the thickness until the temperature at the center of the aluminum holder directly above the ceramic heater agreed with the experimentally measured value there to within 0.01 °C.

Once the thickness of the thermal paste was determined, the simulated temperature profile in the experimental setup was calculated and the temperature difference across the nanofilm/air gap, ΔT, was computed. A sample temperature profile (to scale) from experiment run #18 is shown in Fig. 5.2(b). An important distinction between this chapter and the previous experimental comparisons to theory is the difference between the temperature drop across the nanofilm/air gap, ΔT, and the difference between the heater and chiller setpoints, $\Delta T_{out} = T_{Heater} - T_{Chiller}$. In particular, work by Schäffer [4–6, 15] used ΔT_{out} when comparing their experimentally measured wavelengths to the AP model. As Fig. 5.2(c) shows, ΔT_{out} is much larger than ΔT for these experimental runs. This crucial difference stems from the fact that the nanofilm and air layers are so much smaller than the rest of the components in the setup. This means that even though the thermal conductivities of the other components in the experimental setup are much higher than the polymer and air thermal conductivities (see Table 5.1 for a full listing of thermal conductivities), the vastly larger size of these components leads to sizable temperature drops. These external temperature drops are not incorporated into the theoretical models, so it is vitally important to use ΔT and not ΔT_{out} when comparing experimentally measured wavelengths to the predictions of linear stability analysis.

Figure 5.2: Diagram of the computational domain for the temperature simulations of the redesigned experimental setup

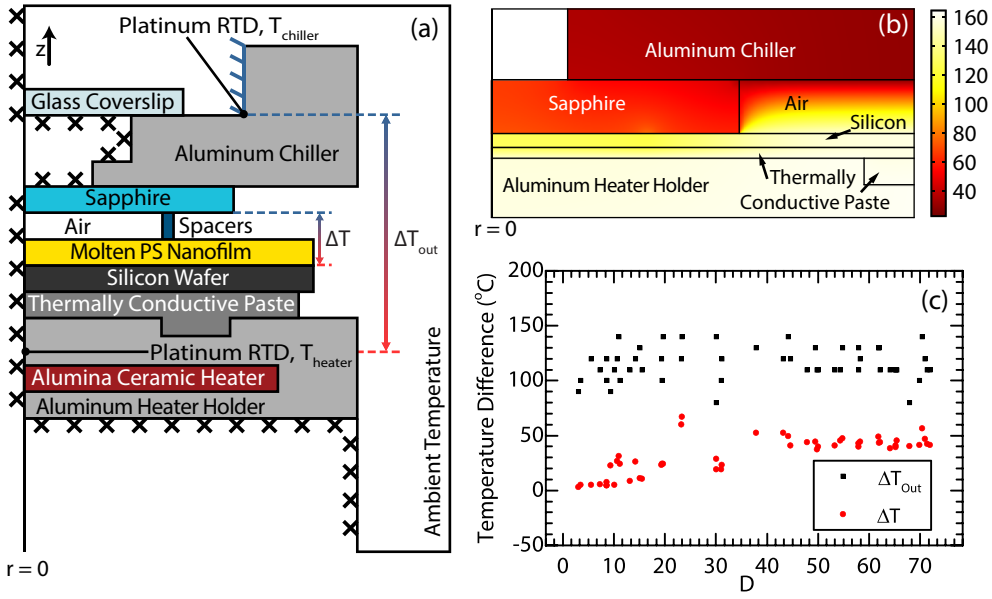

(a) Cylindrically symmetric simulation geometries for computation of the temperature profile within the experimental setup (not drawn to scale). For a complete listing of the sizes and positions of the the components, see Table 5.1. Due to cylindrical symmetry there is no radial thermal flux along the axis of symmetry at $r = 0$, and no thermal flux boundary conditions are denoted by black crosses. The inner vertical edge of the aluminum chiller is treated as an isothermal boundary condition and this is denoted by (blue) slanted lines. The heating is treated as a volumetric source in the alumina ceramic heater whose total power equals the measured electrical power dissipated by the heater. All the remaining exterior boundaries were isothermal boundary conditions set to the measured ambient temperature. (b) Numerical temperature profile of the experimental setup (to scale) as computed with COMSOL from experiment run #18. The nanofilm and spacers are too small to be seen in this figure so they are not labeled. (c) The temperature difference across the nanofilm/air bilayer, ΔT and the temperature difference between setpoints, ΔT_{out} as a function of the normalized separation distance, D, for all the experimental runs.

Table 5.1: Sizes and thermal conductivities for each domain in the numerical simulations of temperature within the experimental setup

Feature	**Inner Radius** (mm)	**Outer Radius** (mm)	**Thickness** (mm)	**Thermal Conductivity** (W/m-°C)
Aluminum chiller	0	57.3	25.4	200 (23.9 – 25 °C) [48]
Aluminum chiller cutout - Large	0	28.7	19.1	0.0257 – 0.0454 (20 – 300 °C) [28]
Aluminum chiller cutout - Medium	0	2.43	4.83	
Aluminum chiller cutout - Small	0	1.47	1.52	
Glass coverslip	0	14.3	0.150	1.09 (23 °C) [29]
Sapphire window	0	4.76	1.02	29.9 (69 °C) [31]
Air gap	0	2.88	d_o - h_o	0.0257 – 0.0454 (20 – 300 °C [28]
SU-8 spacers	2.88	3.13	d_o - h_o	0.300 [32]
PS film	0	25.4	h_o	0.130 (100 °C) [22]
Silicon wafer	0	25.4	0.279	93.9 (127 °C) [33]
Aremco Heataway 638 paste layer	0	r_{paste}	h_{paste}	2.23 [49]
Aremco Heataway 638 paste inset	7.16	14.3	0.508	
Aluminum heater holder	0	43.0	10.2	200 (23.9 – 25 °C) [48]
Alumina ceramic heater	0	14.3	1.10	20.0 (20 °C) [50]

The thermal conductivity of each domain is listed with the temperature found in the literature at which that value was measured. If no temperature is listed, then a temperature for the thermal conductivity measurement could not be found. All thermal conductivities were taken as constant, with the exception of the air domains where a COMSOL built-in material was used which had a temperature dependent thermal conductivity. The values of d_o, h_o, r_{paste}, and h_{paste} for each experimental run can be found in Table 5.5. The thermal paste domain comprises two parts. One part is paste which filled an inset into the aluminum heater holder. This inset was completely filled for every experimental run and was held constant for every simulation. On top of this inset thermal paste was added to form an additional layer which covered the center of the aluminum heater holder. Because the precise amount and distribution of the thermal paste layer was not known, this value was varied so that the temperature at the location of the RTD above the heater matched the value measured in the experimental run (T_{Heater}). The total size of the domain was 192 mm in radius and 254 mm in height. The domain was offset so that the top of the computational domain was 80 mm above the bottom of the aluminum chiller as this was the location of the bounding cardboard box. Note that the domain did not extend into the region directly beneath the aluminum heater holder nor into the region between the glass coverslip and the sapphire window as represented in Fig. 5.2(a). The point which represented the platinum RTD location was set to be on the axis of symmetry at $r = 0$ and 2.54 mm below the top of the aluminum heater holder.

During the finite element simulations, the nanofilm interface is treated as flat and static. Since the models are derived within the context of linear stability the perturbations to the film interface are infinitesimal and as long as measurements of the wavelength are made at early times the interface should be very close to flat. Furthermore, as was mentioned above, the interface can be treated as static in the heat equation due to the vanishingly small product of the Prandtl and Reynolds number. However, during instability growth the interface does deform in time and so the temperature drop across the system should decrease as the instability grows because the overall thermal conductivity of the air/nanofilm bilayer increases as protrusions grow. This increase in thermal conductivity leads to increased thermal flux through the system which is what causes the increased temperature drop. To confirm quantitatively that the temperature drop across the bilayer when the film is flat is very nearly equal to the temperature drop across the bilayer when the film is strongly perturbed, as it would be at late times, we performed additional numerical simulations. Fig. 5.3(a) shows a portion of the computational domain from Fig. 5.2(a) focusing solely on the air/nanofilm bilayer. Correspondingly, Fig. 5.3(b) shows the analogous bilayer interface with a sinusoidal perturbation which represents the film at late times after the protrusions have grown significantly. In the perturbed interface simulations, the rest of the geometry was identical to the simulations presented above. The value of the sinusoidal perturbation was equal to 0.9 h_o for each simulation and the wavelength was set to 50 microns. The sinusoid was chosen so that the maximum occurred at $r = 0$, as depicted in Fig. 5.3(b). The temperature drop in each of these two cases was computed by taking the difference between the value at the nanofilm/silicon interface and the value at the air/sapphire interface, evaluated at $r = 0$. With the perturbed interface, the temperature drop across the bilayer, ΔT_{sin}, is slightly smaller than the temperature drop across the flat interface, ΔT, as seen by the positive values in Fig. 5.3(c). In this figure, the differences in the temperature drops are plotted as a function of $h_o/d_o = D^{-1}$ which represents how much of the gap is filled by the nanofilm. When the nanofilm composes a larger portion of the gap, the perturbation has a stronger effect and so the difference in temperature drops is larger. However, even at the maximum value, the difference between the two techniques is less than 0.2 °C and so we were justified in using a flat interface for the temperature simulations to compute ΔT. Note that these simulations used the experimental parameters for each of the runs listed in Table 5.5. As such, there were multiple runs with the same value of h_o/d_o, but with different heater and chiller setpoints, which led to the observed scatter in Fig. 5.3(c).

Figure 5.3: Effect of a sinusoidal deformation to the molten nanofilm on the temperature simulations of the experimental setup

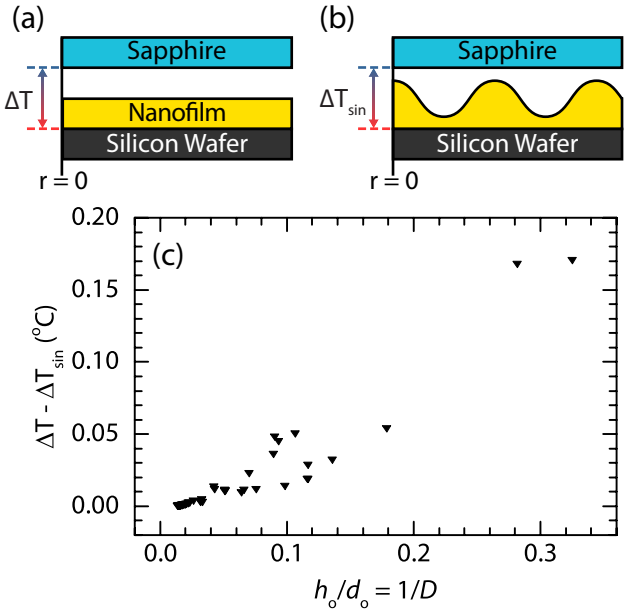

(a) Portion of the cylindrically symmetric simulation geometry from Fig. 5.2(a). (b) Analogous portion of the geometry showing a sinusoidal deformation to the nanofilm/air interface. The simulation geometry except for the deformation to the interface is identical to Fig. 5.2(a). (c) Difference between the computed temperature drop across the bilayer with a flat interface and the temperature drop across the bilayer with a sinusoidally deformed interface plotted as a function of h_o/d_o for each of the experimental runs listed in Table 5.5.

5.4 Image Analysis Process for the Extraction of the Wavelength and Growth Rate of the Fastest Growing Mode

The image analysis process was the defining feature of these experiments because this process yielded the characteristic wavelength, λ_o, and the growth rate, b_o, of the fastest growing mode of the instability. As mentioned above, the functional dependencies of these quantities differentiate the three proposed models and allow us to identify the dominant physical mechanism. As such, we have expanded upon the techniques used in previous instability studies of this system [1, 39] to measure λ_o and b_o. For the wavelength analysis we followed the general approach of previous studies. First, a defect free region was selected for analysis. Then, the 2D discrete Fourier transform of the image was computed. This was then converted to a power spectral density and averaged azimuthally to find the power spectral density as a function of wavevector, k. Then, the peak was determined to find the wavevector of the fastest growing mode which was then converted back to a real space wavelength. The key difference in this chapter was the choice of the fitting function to extract

the peak of the power spectral density. We derived a fitting function, presented below, that incorporated the physics of the hydrodynamic instability that allowed us to extract both the wavelength and the growth rate of the instability from the power spectral density simultaneously. Before detailing the fitting procedure, we will derive the new fitting function and highlight some of its features.

The fitting function used in this chapter to identify the peak of the power spectral density is markedly different than what was used in Ch. 3 or Ref. [1] . Traditionally, the fitting functions have been approximated as either Lorentzian or Gaussian peaks as is typically done in vibrational spectroscopy [51, 52]. However, in vibrational spectroscopy, the use of these peak functions is physically motivated and knowing the source of the signal is integral to the fitting process. For example, the Lorentzian lineshape function arises from the interaction of a driven oscillator with its environment while the Gaussian lineshape function occurs due to instrumental effects or Doppler broadening. To date, the use of these types of functions in the study of hydrodynamic instabilities has been an arbitrary ansatz and so we derived a fitting function based on the physical signal in this system. The details of this derivation will now be presented.

In this system, the intensity of the light reflected from the film was measured by the camera. By treating the polymer layer as an asymmetric Fabry-Pérot etalon, it can be shown that changes in the height of the polymer are linearly proportional to changes of the reflected intensity in the limit of small deformations. From Ref. [53], the reflected fraction of the incident intensity is

$$I_R = \frac{C_1 + C_2 \sin^2(C_4 l)}{C_3 + C_2 \sin^2(C_4 l)}, \tag{5.4}$$

where l is the length of the cavity, and C_1, C_2, C_3, and C_4 are constants which depend on the properties of the etalon, such as the refractive index, optical wavelength, and the reflectivities. Since we are only interested in the proportionality of a change in the cavity length from l to $l + \Delta l$, we can ignore the more complicated forms of these constants. We then take the difference

$$I_R(l + \Delta l) - I_R(l) = \frac{C_1 + C_2 \sin^2(C_4 l + C_4 \Delta l)}{C_3 + C_2 \sin^2(C_4 l + C_4 \Delta l)} - \frac{C_1 + C_2 \sin^2(C_4 l)}{C_3 + C_2 \sin^2(C_4 l)}. \tag{5.5}$$

After simplification, application of trigonometric identities, and a Taylor expansion in the cavity length change, Δl, we see that

$$I_R(l + \Delta l) - I_R(l) = \frac{(C_3 - C_1) \sin(2C_4 l) C_2 C_4 \Delta l}{C_3^2 + 2C_2 C_3 \sin^2(C_4 l) + C_2^2 \sin^4(C_4 l)} \propto \Delta l. \tag{5.6}$$

Thus our measured signal, I, can be expressed as the change of the film height from the initially undisturbed film height

$$I\left(\vec{x},t\right) \propto h\left(\vec{x},t\right) - h_o. \tag{5.7}$$

We used a Fourier series to express the position of the film interface as a function of both time and space so that

$$h(\vec{x},t) = h_o + \sum_{k'} \delta h_{k'} e^{i\vec{k'}\cdot\vec{x}} e^{b_{k'}t}. \tag{5.8}$$

In this expression, $\vec{k'}$ is a wavevector, $\delta h_{k'}$ are the Fourier coefficients that describe the configuration of the interface, and $b_{k'}$ is the (real) growth rate associated with the wavevector $\vec{k'}$. Substituting Eq. (5.8) into Eq. (5.7) yields

$$I\left(\vec{x},t\right) \propto \sum_{k'} \delta h_{k'} e^{i\vec{k'}\cdot\vec{x}} e^{b_{k'}t}. \tag{5.9}$$

We took the Fourier transform of the intensity

$$\tilde{I}\left(\vec{k},t\right) \propto \sum_{k'} \delta h_{k'} e^{b_{k'}t} \int_{-\infty}^{\infty} e^{i\vec{k'}\cdot\vec{x}} e^{-i\vec{k}\cdot\vec{x}} dx = \sum_{k} \delta h_k e^{b_k t}. \tag{5.10}$$

In the limit of a system which is infinite in lateral extent, the wavevectors will be infinitesimally close together and this sum becomes a continuous function of k

$$\tilde{I}\left(\vec{k},t\right) \propto e^{b(k)t}, \tag{5.11}$$

where $b\left(k\right)$ is the full dispersion relation derived from linear stability analysis. Then the power spectral density, $S\left(\vec{k},t\right)$, will be

$$S\left(\vec{k},t\right) \propto \left|\tilde{I}\left(\vec{k},t\right)\right|^2 = e^{2b(k)t}. \tag{5.12}$$

While the specific form of the dispersion relation varies depending on the model chosen to describe the instability, this sort of fitting function should fit the power spectral density of any hydrodynamic instability provided that the appropriate dispersion relation is inserted into Eq. (5.12). In the case of the present instability there is a common thread that unites all three proposed mechanisms and allows us

to define a generic fitting function that was used to find the wavelength and growth rate. Specifically, all the models have dispersion relations of the form

$$b(k) = C_1 k^2 - C_2 k^4, \tag{5.13}$$

where C_1 and C_2 are constants that depend on the specific model. However, the location of the maximum growth rate, k_o, is always

$$k_o = \sqrt{\frac{C_1}{2C_2}}. \tag{5.14}$$

Substituting k_o back into Eq. (5.13) yields the maximum growth rate, b_o,

$$b_o = b(k_o) = \frac{C_1^2}{4C_2}. \tag{5.15}$$

If we now factor this out of Eq. (5.13) then

$$b(k) = b_o \left(\frac{k}{k_o}\right)^2 \left[2 - \left(\frac{k}{k_o}\right)^2\right]. \tag{5.16}$$

Inspired by these results, we will fit the peak in the power spectral density with a function of the form

$$\mathcal{F}(k,t) = A \exp\left(2b_o t \left(\frac{k}{k_o}\right)^2 \left[2 - \left(\frac{k}{k_o}\right)^2\right]\right). \tag{5.17}$$

In this expression, there are three fitting parameters which were varied to achieve good fits to the peak of the power spectral density. k_o was a fitting parameter which describes the location of the peak and can be converted back to the real space characteristic wavelength using $\lambda_o = 2\pi/k_o$. b_o was a fitting parameter which describes the width of the peak and is equal to the growth rate at the time t. A was the fitting parameter which describes the amplitude of the peak.

There are several interesting things to note about this fitting function when comparing it to the traditional Gaussian or Lorentzian peaks. First, Eq. (5.17) is not symmetric about the peak ($k = k_o$). This follows from the fact that the dispersion relation is not symmetric about its maximum value. To illustrate this point, Fig. 5.4(a) shows the dispersion relation from Eq. (5.16). Returning to the full fitting function in Eq. (5.17), we denote the half maximum points of the peak by k_- and k_+ and they have the forms

$$k_- = k_o \sqrt{1 - \sqrt{\frac{\ln 2}{2b_o t}}}, \tag{5.18}$$

$$k_+ = k_o\sqrt{1+\sqrt{\frac{\ln 2}{2b_o t}}}. \tag{5.19}$$

Additionally, there is a temporal dependence to Eq. (5.17) and the peak gets taller and sharper in time, as Fig. 5.4(b) shows. In Fig. 5.4(b), we have set $A = 1$ for visualization purposes. Notice that there are two points where $b = 0$ (at $k/k_o = 0$ and $k_c/k_o = \sqrt{2}$) and those points do not move in time, regardless of the shape of the rest of the curve. We also compared this fitting function to the Gaussian and Lorentzian peak shapes in Fig. 5.4(c). The $t = 1.00/b_o$ curve from Fig. 5.4(b) was normalized by its maximum value and a nonlinear least squares fit was performed in OriginPro 2015[54] with Gaussian and Lorentzian functions of the forms

$$\mathcal{G}(k) = \frac{A_g}{w_g\sqrt{\pi/2}}\exp\left[-2\left(\frac{k-k_g}{w_g}\right)^2\right] + C_g, \tag{5.20}$$

$$\mathcal{L}(k) = \frac{2A_l}{\pi}\frac{w_l}{4(k-k_l)^2 + w_l^2} + C_l. \tag{5.21}$$

A full listing of the fitted parameters can be found in the caption of Fig. 5.4. The Gaussian and Lorentzian curves generally fit the peak moderately well, but the location of the peak is 5% smaller than the actual peak and this discrepancy highlights the need for a fitting function that accurately captures the physics of the underlying process.

With this new analysis tool opening a wider range of possibilities, we turned to the image analysis and fitting process. To begin, a region free of dust in the film or surface inhomogeneities was selected from the time series of experimental images. Previously, it had been shown that the presence of defects in the film can shift the location of the peak in the power spectrum, particularly at early times [39]. The size of the region selected for each experimental run can be found in Table 5.6. Next, the time series from a single filter wavelength was selected. Depending on the initial film thickness, h_o, and the total gap thickness, d_o, the features showed differing levels of contrast for different filters and in some cases showed a large degree of saturation. As such, the time series which showed the largest contrast was selected for further analysis and the choice for every experimental run is listed in Table 5.6.

Since the predictions for λ_o and b_o presented in Eqs. (5.23) to (5.28) were based upon the assumption of an infinitesimal perturbation, it is important that the images

Figure 5.4: Plots of the derived peak fitting function and comparison to Gaussian and Lorentzian peaks

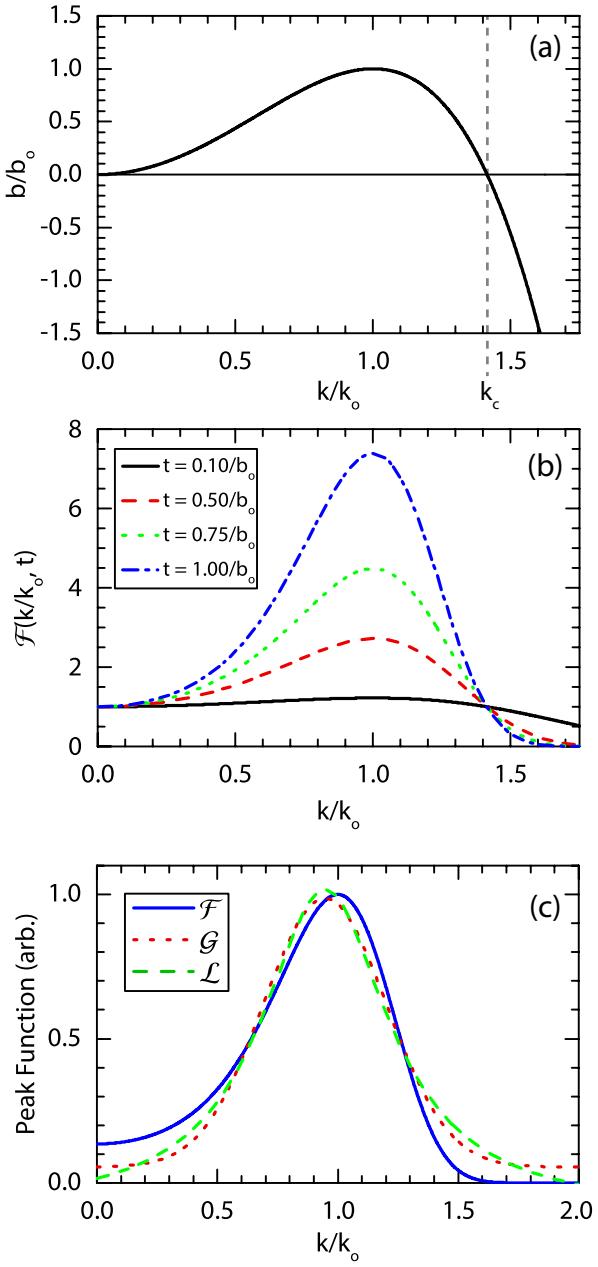

(a) Plot of the normalized dispersion relation, b/b_o, as a function of normalized wavevector, k/k_o. (b) Plot of Eq. (5.17) as a function of normalized wavevector at several different times. (c) Plot of Eq. (5.17) at $t = 1.00/b_o$ normalized to unity and fit by Gaussian, $\mathcal{G}$, and Lorentzian, $\mathcal{L}$, peaks. The Gaussian peak is the (red) dotted line and the Lorentzian peak is the (green) dashed line. The equations for these peaks are found in Eqs. (5.20) and (5.21), respectively. The parameters for the Gaussian fit were A_g = 0.596, w_g = 0.510, k_g = 0.947, and C_g = 0.0549. The parameters for the Lorentzian fit were A_l = 1.14, w_l = 0.646, k_l = 0.947, and C_l = -0.102.

are analyzed at the earliest possible times. A previous instability wavelength study [39] had used a background subtraction technique where an early time image which did not show any signs of instability was subtracted from all the later images in the time series to highlight the instability and remove any static background features. While the background subtraction technique worked well in that instance, it proved ineffectual for the present analysis for two reasons. The first reason was the presence of large scale interference fringes that slowly moved in the longer experimental runs. This study examined a larger area than had previously been accessible due to improved film preparation procedures and a better experimental setup. This meant that there were more fringes in the image for a given level of parallelism as compared to previous work. These fringes were much larger than the characteristic spacing of the instability, but still form an unwanted background signal in the power spectral density. Additionally, a much larger section of parameter space was examined and in certain regions the instability took a long time to develop, with some runs in excess of 8 hours. With these long evolution times the setup could settle and equilibrate over a long time, leading to slight shifts in the parallelism. Table 5.6 lists the total time elapsed in each experimental run, t_{final}. In most cases t_{final} coincided with the end of the experimental run, particularly for the longer runs. However, there were experimental runs where t_{final} occurred before the end of heating due to large amplitude peak growth which created interference fringes within the peaks themselves. These small scale interference fringes posed difficulties when computing the power spectral density because they added an extra peak at k values slightly larger than k_o. Moreover, if the peak growth was large enough to have interference fringes (> 100 nm) then we should have identified the instability wavelength earlier in the time series to more closely match the predictions of linear stability analysis and fulfill the assumption of an early time measurement. The second and more important issue is that the growth rate measurements are extracted from Eq. (5.17) based on the width of the peak. As a result, any image processing technique which changes the width of the peak will effect the measured growth rate. This caused us to eschew traditional techniques such as thresholding or the top-hat transform and perform computations directly on the raw image.

For each image in the time series of each experimental run, the mean of the image was subtracted to suppress the constant term in the Fourier spectrum. After subtraction of the mean, the two-dimensional discrete Fourier transform of the image was computed using MATLAB [25]. The absolute magnitude of this result was squared to find the power spectral density. We found that a major source of background came from

low frequency components in the vertical and horizontal directions which generally stemmed from nonuniform illumination or very large scale interference fringes. These manifested themselves as a large cross in the 2D power spectral density which caused extra background during the azimuthal average. To reduce this contribution, the values at both $k_x = 0$ and $k_y = 0$ were selected and these values were excluded from the azimuthal average. The remaining values were then averaged azimuthally to produce the power spectral density as a function of wavevector, $k = |\vec{k}|$. Because the images were not processed before the Fourier transform was computed, they showed a fair amount of noise with a large peak at small wavevectors. The peak was easily distinguishable near t_{final}, and so we defined a hard bandpass filter and only selected wavevectors between $k_{\max}$ and $k_{\min}$. The value of $k_{\max}$ was kept constant for every experimental run at $k_{\max} = 0.628\ 1/\mu\text{m}$ and simply served to remove any high frequency pixel noise from the camera. The value of $k_{\min}$ was chosen to be lower than the edge of the peak at t_{final} so that no part of the peak was removed. This was critical to the fitting process because the routines could not accurately fit parameters which were different by many orders of magnitude. To allow automation of the fitting process between all experimental runs, the power spectral densities derived from the time series of processed experimental images were normalized to the maximum value of the power spectral density at t_{final} for that experimental run. The image at t_{final} had the power spectral density with the largest magnitude for a given run because the instability was most well developed at that point. The end result of this step is a normalized plot of the power spectral density as a function of k for each image in the time series which were fit to find the peak wavevector. The fitting procedure fit the peak and the background simultaneously and the background was assumed to be Gaussian in nature and centered at $k = 0$. This assumption is that the very long wavelength interference fringes make up the majority of the background and that they were broadened by the pixelation and noise from the camera. As such, the complete fitting function had the form

$$W(k) \equiv \mathcal{G}(k)+\mathcal{F}(k) = A_g \exp\left[-C_g k^2\right]+A \exp\left(2b_o t\left(\frac{k}{k_o}\right)^2\left[2-\left(\frac{k}{k_o}\right)^2\right]\right). \quad (5.22)$$

In a manner similar to our previous work [39], the image analysis procedure started by fitting the power spectral density at t_{final} and then using those fitting parameters to fit the power spectral density of the image immediately proceeding t_{final}. This procedure continued iteratively for all images in the time series working backwards in time towards the first image in the time series. The initial fit at t_{final} was the

most difficult to converge and was quite sensitive to the initial values of the fitting parameters. Because the process was automated, we imposed a set of requirements to ensure that a converged fit was not spurious and that a valid peak truly existed. Specifically, we required that:

- The standard error on the fitted parameters k_o and b_o was not larger than the parameters themselves.
- The system had reached its steady state temperature: $t > 5$ min.
- Peak half maximum points must be within the bandpass filter bounds: $k_+ < k_{\max}$ and $k_- > k_{\min}$.
- Peak full width at half maximum $(k_+ - k_-)$ must be greater than the distance between consecutive wavevector points.
- At k_o, the peak must be greater than or equal to the background Gaussian: $\mathcal{F}(k_o) \geq \mathcal{G}(k_o)$
- At $k_\pm$, the peak must be greater than or equal to one half the background Gaussian: $\mathcal{F}(k_\pm) \geq \frac{1}{2}\mathcal{G}(k_\pm)$
- The whole fitting function must not be greater than 10 times the maximum of the peak anywhere: $\max[W(k)] < 10\mathcal{F}(k_o)$

These conditions serve to remove fits which numerically converged but were not physical, such as a very tall and narrow peak which was smaller than the distance between points. They also removed fits where the width of the peak is not well determined such as when the half maximum points are outside the fitted range of the bandpass filter. Once this process was completed for every image in a given experimental run, the reported values for k_o and b_o were taken as the earliest time at which a valid fit occurred.

To demonstrate this process on actual experimental data, Fig. 5.5 shows the application of this algorithm to experiment #18. For this experiment, the pictures taken with the 488 nm filter showed the largest contrast, so these were selected for the wavelength and growth rate extraction process and three pictures from the time series are shown in Fig. 5.5(a). Directly beneath each image from Fig. 5.5(a) the natural log of the 2D power spectral density is plotted. The natural log was taken to enhance the contrast of the dark ring, which is the signal of the instability. The

Table 5.2: Fitting constants for the curves shown in Fig. 5.5(c)

Time (min)	$A_g \times 10^{-2}$	$C_g(\mu\text{m}^2)$	$A \times 10^{-5}$	$b_o \times 10^{-3}$(1/min)	$k_o(\text{rad}/\mu\text{m})$
12	4.34	327	49.7	1.56	0.138
16	0.399	32.0	0.619	4.03	0.134
20	0.656	26.9	1.42	3.45	0.133
24	1.37	24.0	1.69	3.28	0.132
29	4.48	22.3	1.31	3.21	0.132

radius of the ring is related to the wavevector and the width of the ring is related to the growth rate. The vertical and horizontal white lines in each image of Fig. 5.5(b) are the regions which were removed to reduce the background due to nonuniform illumination effects. These clearly do not strongly effect the azimuthal average as the ring is visible in all three images and shows rotational symmetry. In contrast to Fig. 3.2(c) where incipient hexagonal order is evident, the images in Fig. 5.5(b) show an azimuthally symmetric ring. That fact that there is no superposed pattern on the ring suggests that these analysis images are from early times before the onset of nonlinear interaction between modes. Next, the 2D plots from Fig. 5.5(b) were azimuthally averaged to produce the curves in Fig. 5.5(c) where the power spectral density is plotted as a function of the magnitude of the wavevector, k. All the curves have been normalized by the maximum value of the power spectral density at t_{final}, which was 29 minutes for this experiment. As was expected, the amplitude of the peak increases as the instability grows in time. The parameters for the curve fits can be found in Table 5.2. Finally, the location of the peak was plotted as a function of time in Fig. 5.5(d). The vertical bars are not error bars, but instead denote the full width at half maximum of the peak as computed from k_- and k_+ in Eqs. (5.18) and (5.19), respectively.

One question that has persisted through earlier work [1, 39] is whether the wavevector (or equivalently, the wavelength) changes systematically as a function of time. At very late times, coarsening is expected to occur and will cause the characteristic wavelength to increase over time. However, within the confines of linear stability there is no expectation of time dependent behavior because the perturbation is assumed to be infinitesimal. Within the context of this chapter, we looked at the

Figure 5.5: Illustration of the image analysis process using the derived fitting function

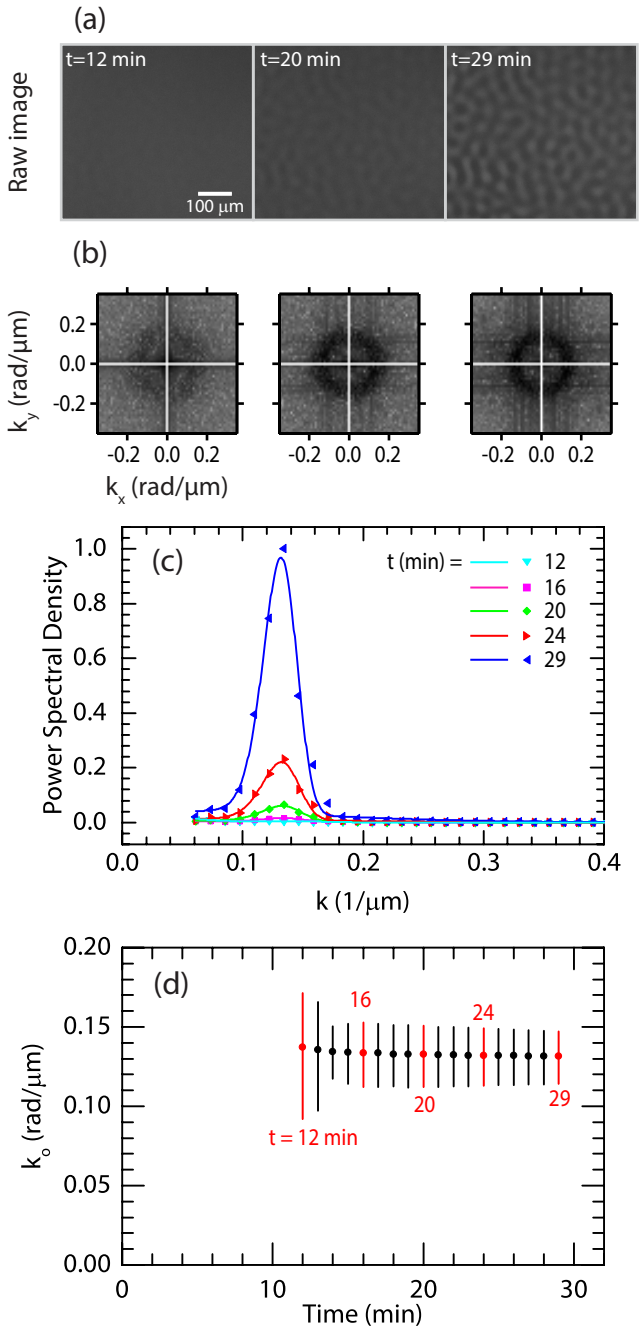

(a) Raw images from experiment #18 taken under 488 nm illumination. (b) Natural log of the 2D power spectral density of the corresponding raw images from (a). The white lines are the regions which were removed to reduce background. (c) Azimuthally averaged power spectral density as a function of wavevector, k (points) and the corresponding fits (solid lines). A full listing of the fit parameters can be found in Table 5.2. (d) Peak location, k_o, as a function of time for experiment #18. The vertical bars represent the full width at half maximum of the peak, as defined by k_- and k_+ in Eqs. (5.18) and (5.19), respectively.

Figure 5.6: Normalized wavevector plotted as a function of time for every experimental run

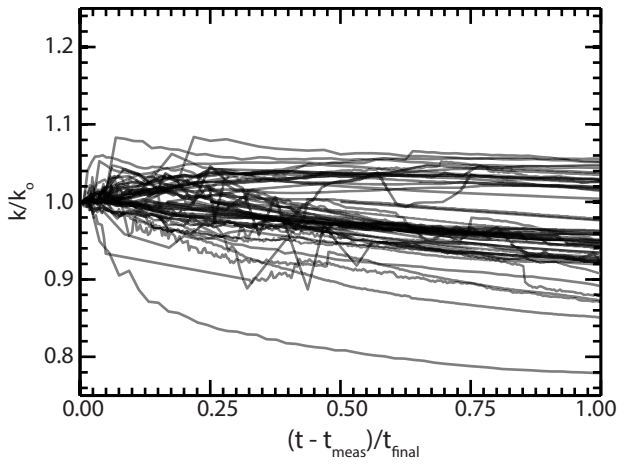

Normalized wavectors as a function of normalized time for every experimental run. The wavevectors were normalized by the first measured peak location, k_o. The times were shifted by subtracting the initial measurement time, t_{meas}, and then normalized by the final time, t_{final}. Each curve is semitransparent and so the darker regions are areas where multiple curves overlap.

temporal dependence of the wavevector for every experiment to see if there was a discernible trend. To do this, the wavector data as a function of time which was plotted in Fig. 5.5(d) was aggregated for all the experimental runs and then normalized. To promote comparison between experiments which could span very different length and time scales, the wavevectors were normalized by the initially measured value, k_o and the times were shifted by the time of the initial wavelength measurement, t_{meas}, so that they all started at the same point. Then each time series was scaled by the final time, t_{final}, so that the curves spanned the same range. The resulting curves were plotted in Fig. 5.6. Generally, there seems to be little systematic shift, as the mean of the normalized wavector at a t_{final} is 0.961, very close to the value of 1 which would be expected if the results were evenly distributed about the initial value. Furthermore, the curves do not show large slopes, particularly at late times. This suggests that the measured wavevectors are relatively constant to within an uncertainty of approximately ± 10%.

5.5 Comparison of Experimental Results to Proposed Mechanisms

With the wavelengths and growth rates computed for all the experimental runs, the experimental data was then compared to the theoretical predictions detailed in Ch. 2. Three models have been proposed to describe this instability [2–6, 8, 10, 15], and each model hypothesized a different destabilizing mechanism to overcome the

Figure 5.7: Diagram of the instability geometry

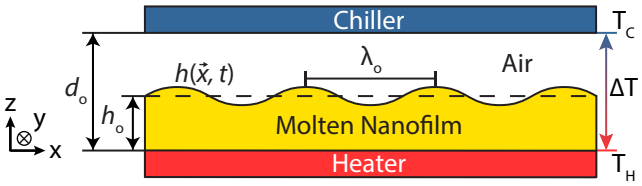

Diagram of the instability geometry (not to scale). In the literature [1–6, 15], the initial film thickness, h_o ranges from 50 to 390 nm; the total gap width, d_o ranges from 100 to 2360 nm; the measured characteristic wavelength, λ_o, ranges from 1.0 to 58 μm; and the temperature drop, ΔT, ranges from 11 to 46 °C.

stabilizing pressure due to surface tension. In each case, the models derive a thin film interface equation from the Navier-Stokes equations using the long-wavelength approximation. Most importantly for the present analysis, they each put forward a prediction for the experimentally measured wavelength, λ_o, and the corresponding growth rate of that wavelength, b_o, within linear stability analysis. While each of these models has been treated in detail previously, we will summarize them briefly in the following section and then scale them so that it is easier to differentiate them with the experimental data that is presented below. Note that in previous studies [1], the SC model had been effectively eliminated due to its lack of temperature dependence. We concur with this assessment, but still make comparisons to the SC model for completeness and to lend further support to the conclusion that it does not play a dominant role in this system.

5.5.1 Wavelength and Growth Rate from Three Proposed Instability Models

While each of these models has been treated in depth previously, we briefly summarize them and restate their expressions for the wavelength and growth rate. Each proposed model considered a simplified geometry which is shown in Fig. 5.7. The initial film thickness, h_o, is typically on the order of 100 nanometers and the distance from the heated substrate to the cooled plate, d_o, is typically on the order of microns. The temperature difference between the bottom of the nanofilm and the top of the air layer, ΔT, is typically on the order of a few degrees Celsius. The spontaneous deformations of the instability have a characteristic wavelength, λ_o, which is usually on the order of 10 microns and this relatively large value compared to the film thickness justifies the use of the long wavelength approximation.

Surface Charge (SC) Model

The SC model, developed by Chou and Zhuang [2, 3], is based upon a destabilizing electrostatic pressure. They hypothesized that charges at the nanofilm's free interface with the air, $h(\vec{x}, t)$ in Fig. 5.7), induce image charges in the heating and cooling plates. The combined effect of these charges is a destabilizing electrostatic pressure. The characteristic wavelength and growth rate in the SC model are

$$\frac{\lambda_o^{\mathrm{SC}}}{2\pi h_o} = \sqrt{\frac{2\varepsilon_o \varepsilon_p^2 \gamma}{\sigma^2 h_o D^2}} \left(D + \frac{1}{\varepsilon_p} - 1 \right)^{3/2}, \tag{5.23}$$

$$b_o^{\mathrm{SC}} = \frac{\sigma^4 h_o D^4}{12\mu\gamma\varepsilon_o^2\varepsilon_p^4 h_o^3} \left(D + \frac{1}{\varepsilon_p} - 1 \right)^{-6}. \tag{5.24}$$

In these expressions, h_o is the initial film thickness, ε_o is the permittivity of free space, ε_p is the permittivity of the nanofilm, γ is the surface tension of the molten nanofilm, σ is the interfacial charge density, μ is the viscosity of the nanofilm, and $D \equiv d_o/h_o$ is the normalized separation distance. A listing of the range of material and experimental parameters can be found in Table 5.3 for 1.1k M_W polystyrene (PS) which composes the nanofilms used in this study. Within all three of these models, the dependence of the material properties on temperature and electric field was treated as a higher order effect, with the notable exception of the surface tension in the thermocapillary model where it is explicitly included as the driving force. As such, all material properties were evaluated at the temperature of the nanofilm/air interface for each experiment. A full listing of the material properties for every experimental run can be found in Table 5.7.

Acoustic Phonon (AP) Model

Next, Schäffer *et al.* proposed the AP model [4–6, 15]. In this model, acoustic phonon reflections from every interface create a net acoustic pressure which destabilizes the interface and causes protrusions to grow. In the AP model, the characteristic wavelength and growth rate are

$$\frac{\lambda_o^{\mathrm{AP}}}{2\pi h_o} = \sqrt{\frac{\gamma u_p}{Q(1-\kappa)k_a \Delta \mathrm{T}}} \left(D + \kappa - 1 \right), \tag{5.25}$$

$$b_o^{\mathrm{AP}} = \frac{[Q(1-\kappa)k_a \Delta \mathrm{T}]^2}{3\mu\gamma u_p^2 h_o} \left(D + \kappa - 1 \right)^{-4}. \tag{5.26}$$

In addition to the parameters defined after Eqs. (5.23) and (5.24), Q is the acoustic phonon quality factor and is related to how much momentum is reflected by the interfaces, u_p is the speed of sound in the polymer, k_a is the thermal conductivity of air, and κ is the ratio of the thermal conductivities of the air and polymer layers. The values of these parameters and material properties can be found in Table 5.3 and Table 5.7.

Thermocapillary (TC) Model

Several years later, Dietzel and Troian proposed a model based on interfacial thermocapillary stresses [8, 10]. For a single component fluid, the surface tension must decrease as a function of temperature. Protrusions will be slightly cooler than valleys and they will have a correspondingly higher surface tension. The gradient in surface tension along the interface creates a destabilizing shear stress which causes growth. For the TC model, the characteristic wavelength and growth rate have the form

$$\frac{\lambda_o^{\mathrm{TC}}}{2\pi h_o} = \sqrt{\frac{4\gamma}{3\kappa\gamma_{\mathrm{T}}\Delta\mathrm{T}}}\left(\sqrt{D} + \frac{(\kappa-1)}{\sqrt{D}}\right), \tag{5.27}$$

$$b_o^{\mathrm{TC}} = \frac{3\left(\kappa\gamma_{\mathrm{T}}\Delta\mathrm{T}\right)^2}{16\mu\gamma h_o}\left(\sqrt{D} + \frac{(\kappa-1)}{\sqrt{D}}\right)^{-4}, \tag{5.28}$$

where γ_{T} is the thermocapillary coefficient, which is the absolute value of the derivative of the surface tension as a function of temperature. The values of these parameters and material properties can be found in Table 5.3 and Table 5.7.

5.5.2 Summary of Scaled Wavelength and Growth Rate Predictions from Proposed Models

Since each proposed model has a distinct mechanism, they each have different predictions for the functional forms of the wavelength and the growth rate. To investigate these differences systematically, each quantity can be scaled to isolate the dependence of the wavelength and growth rate on a single experimentally controlled parameter. In this chapter, we will focus on the normalized separation distance, $D \equiv d_o/h_o$, and the temperature drop, $\Delta\mathrm{T}$, as the two parameters which will be extensively varied. These parameters have the advantage that they are relatively easy to tune experimentally while keeping the same nanofilm material. This allows us to minimize uncertainties in the material properties while still probing the proposed models. In particular, we define the scaled quantities shown in Table 5.4. With these scaled quantities, the different functional dependencies provide a clean way

Table 5.3: Parameters for the experimental runs and material properties for 1.1k M_W polystyrene

h_o	Initial nanofilm thickness	96 – 352 nm
d_o	Gap width	826 – 7150 nm
D	Normalized separation distance	3.08 – 71.9
ΔT	Temperature drop across bilayer	3.6 – 67.2 °C
ε_o	Permittivity of free space	8.85×10^{-12} F/m
ε_p	Nanofilm relative permittivity	3.5
σ	Interfacial charge density	1 – 3 mC/m^2 [3]
μ	Viscosity	2 – 8030 Pa $\cdot$ s [24]
u_p	Speed of sound in nanofilm	1850 m/s [21]
Q	Acoustic phonon quality factor	6 [4–6, 15]
k_a	Air thermal conductivity	28.9 – 34.5 mW/m-°C [23]
k_p	Nanofilm thermal conductivity	120 – 129 mW/m-°C [22]
κ	Thermal conductivity ratio	0.23 – 0.27
γ	Surface tension	29.3 – 35.8 mN/m [22]
γ_{T}	Thermocapillary coefficient	79 μN/(°C-m) [22]

More details of the experimental parameters for each run can be found in Tables 5.5, 5.6, and 5.7. This table contains all the material parameters necessary to evaluate the wavelength and growth rate predictions for all three models.

to differentiate between the three models. For instance, note that the SC model has no temperature dependence, and so it can be readily distinguished from the other two models by investigating $\Lambda_{\Delta\mathrm{T}}^{\mathrm{SC}}$ and $\beta_{\Delta\mathrm{T}}^{\mathrm{SC}}$. The AP and TC models show a similar temperature dependence in $\Lambda_{\Delta\mathrm{T}}^{\mathrm{AP}}$ and $\Lambda_{\Delta\mathrm{T}}^{\mathrm{TC}}$, but they can be distinguished using the functional dependencies of Λ_D^{AP} and Λ_D^{TC} instead. Using all these expressions will allow us to provide a more complete and extensive comparison between experimental measurements and the predictions of linear stability than has been done previously.

Note that the way the normalization for the wavelengths and growth rates is different in Table 5.4 than the normalizations used in Ch. 3 and Ch. 4. In those chapters, the quantities, C^{AP} and C^{TC}, encapsulated all the material properties of the system and were treated as fitting parameters for each model. The groupings of the material

Table 5.4: Scaled wavelengths, Λ, and growth rates, β, for each of the proposed models

SC Model

$$\Lambda_D^{\mathrm{SC}} \equiv \frac{\lambda_o^{\mathrm{SC}}}{2\pi\sqrt{h_o}}\sqrt{\frac{\sigma^2}{2\varepsilon_o\varepsilon_p^2\gamma}} = \frac{\left(D+\varepsilon_p^{-1}-1\right)^{3/2}}{D} \qquad \beta_D^{\mathrm{SC}} \equiv \left(\frac{2\varepsilon_o\varepsilon_p^2\gamma}{\sigma^2}\right)^2 \frac{3b_o^{\mathrm{SC}}\mu}{h_o\gamma} = \frac{D^4}{\left(D+\varepsilon_p^{-1}-1\right)^6}$$

$$\Lambda_{\Delta\mathrm{T}}^{\mathrm{SC}} \equiv \frac{\lambda_o^{\mathrm{SC}} D}{2\pi\sqrt{h_o}\left(D+\varepsilon_p^{-1}-1\right)^{3/2}}\sqrt{\frac{\sigma^2}{2\varepsilon_o\varepsilon_p^2\gamma}} = 1 \qquad \beta_{\Delta\mathrm{T}}^{\mathrm{SC}} \equiv \left(\frac{2\varepsilon_o\varepsilon_p^2\gamma}{\sigma^2}\right)^2 \frac{3b_o^{\mathrm{SC}}\mu\left(D+\varepsilon_p^{-1}-1\right)^6}{h_o\gamma D^4} = 1$$

AP Model

$$\Lambda_D^{\mathrm{AP}} \equiv \frac{\lambda_o^{\mathrm{AP}}\sqrt{\Delta\mathrm{T}}}{2\pi h_o}\sqrt{\frac{Q(1-\kappa)k_a}{\gamma u_p}} = D+\kappa-1 \qquad \beta_D^{\mathrm{AP}} \equiv \frac{\left(\gamma u_p\right)^2 3b_o^{\mathrm{AP}}\mu h_o}{\left(Q(1-\kappa)k_a\right)^2\gamma(\Delta\mathrm{T})^2} = \frac{1}{(D+\kappa-1)^4}$$

$$\Lambda_{\Delta\mathrm{T}}^{\mathrm{AP}} \equiv \frac{\lambda_o^{\mathrm{AP}}}{2\pi h_o\left(D+\kappa-1\right)}\sqrt{\frac{Q(1-\kappa)k_a}{\gamma u_p}} = \frac{1}{\sqrt{\Delta\mathrm{T}}} \qquad \beta_{\Delta\mathrm{T}}^{\mathrm{AP}} \equiv \frac{\left(\gamma u_p\right)^2 3b_o^{\mathrm{AP}}\mu h_o\left(D+\kappa-1\right)^4}{\left(Q(1-\kappa)k_a\right)^2\gamma} = (\Delta\mathrm{T})^2$$

TC Model

$$\Lambda_D^{\mathrm{TC}} \equiv \frac{\lambda_o^{\mathrm{TC}}\sqrt{\Delta\mathrm{T}}}{2\pi h_o}\sqrt{\frac{3\kappa\gamma_{\mathrm{T}}}{4\gamma}} = \frac{D+\kappa-1}{\sqrt{D}} \qquad \beta_D^{\mathrm{TC}} \equiv \left(\frac{4\gamma}{3\kappa\gamma_{\mathrm{T}}}\right)^2 \frac{3b_o^{\mathrm{TC}}\mu h_o}{\gamma(\Delta\mathrm{T})^2} = \frac{D^2}{(D+\kappa-1)^4}$$

$$\Lambda_{\Delta\mathrm{T}}^{\mathrm{TC}} \equiv \frac{\lambda_o^{\mathrm{TC}}\sqrt{D}}{2\pi h_o\left(D+\kappa-1\right)}\sqrt{\frac{3\kappa\gamma_{\mathrm{T}}}{4\gamma}} = \frac{1}{\sqrt{\Delta\mathrm{T}}} \qquad \beta_{\Delta\mathrm{T}}^{\mathrm{TC}} \equiv \left(\frac{4\gamma}{3\kappa\gamma_{\mathrm{T}}}\right)^2 \frac{3b_o^{\mathrm{TC}}\mu h_o\left(D+\kappa-1\right)^4}{\gamma D^2} = (\Delta\mathrm{T})^2$$

properties for each model had the forms

$$C^{\mathrm{SC}} = 2\pi\sqrt{\frac{2\varepsilon_o\varepsilon_p^2\gamma}{\sigma^2}}, \tag{5.29}$$

$$C^{\mathrm{AP}} = 2\pi\sqrt{\frac{\gamma u_p}{Q(1-\kappa)k_a}}, \tag{5.30}$$

$$C^{\mathrm{TC}} = 2\pi\sqrt{\frac{4\gamma}{3\kappa\gamma_{\mathrm{T}}}}. \tag{5.31}$$

However, treating these quantities as a fitting parameter neglects the fact that each of the material properties has a temperature dependence that varies between experimental runs. This technique has the limitation that it requires the material parameters, such as γ or k_p, to be constant across every experimental run to be able to fit the functional form with the constants C^{AP} and C^{TC}, which depend on material properties, but not D or $\Delta\mathrm{T}$. However, we know empirically that these "constants"

show variation with temperature because their constituents do. A full listing of the material properties for each experimental run can be found in Table 5.7 to illustrate the ranges over which the parameters vary. Since we are scanning a much larger range of experimental parameters than in previous work, we wanted to do a more rigorous treatment of the variation in material properties between experimental runs. To remedy this issue, we chose to scale the expressions in Table 5.4 so that almost all of the material properties were absorbed into the scaled wavelength or scaled growth rate on the left hand side of the equation and then plot this quantity against the remaining experimentally tunable parameters on the right hand side. Plotted in this way, all the points for a given normalization should lie on a line with slope equal to one. We first turn to the wavelength scalings for each model and then transition to the growth rate scalings to examine the correspondence between the scaled experimental data and the predictions of the proposed models.

5.5.3 Nondimensional Wavelength Comparisons

For each of the three proposed models, we isolated the dependence of the wavelength on both the normalized gap separation distance, D, and the temperature drop, ΔT. Generally, the SC model is distinguished by the lack of dependence on ΔT while the AP and TC models can be most easily distinguished by the difference in the predicted dependence on D. A full listing of the scaled wavelengths can be found in the middle column of Table 5.4. Tables 5.5, 5.6, and 5.7 contain all the experimental parameters, material properties, and derived values for each run.

We first scaled the wavelength prediction of the SC model from Eq. (5.23) to yield Λ_D^{SC} and $\Lambda_{\Delta T}^{SC}$. The results of these scalings are shown in Fig. 5.8. For both Fig. 5.8(a) and Fig. 5.8(b), the solid line represents the expected relationship from the theoretical prediction with no adjustable fitting parameters. Neither scaling for the experimental data shows good agreement with the predictions of the SC model, as Λ_D^{SC} shows a generally constant behavior when it should be linear in Fig. 5.8(a) and $\Lambda_{\Delta T}^{SC}$ shows a decay with increasing ΔT when it should be constant in Fig. 5.8(b).

Next, we scaled the wavelength prediction of the AP model from Eq. (5.25) to yield Λ_D^{AP} and $\Lambda_{\Delta T}^{AP}$ and the results are shown in Fig. 5.9. As in Fig. 5.8, the solid line is the expected functional dependence for the theoretical prediction with no adjustable parameters. In Fig. 5.9(a), the behavior of Λ_D^{AP} shows a significant departure from linearity at larger values of $D + \kappa - 1$. The behavior of $\Lambda_{\Delta T}^{AP}$ in Fig. 5.9(b) is more linear and much closer to the predictions of the AP model, although there are some

Figure 5.8: Wavelengths normalized by the SC model

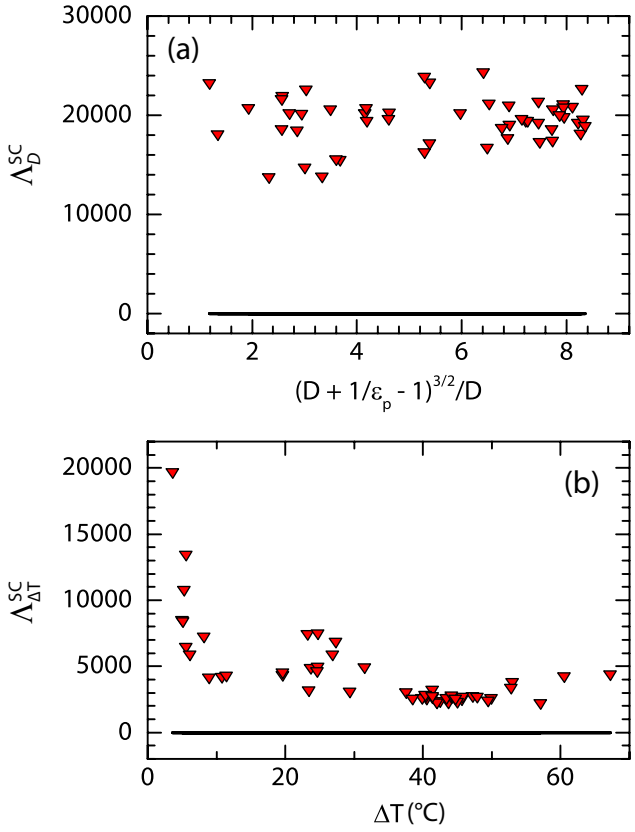

In each case, the (black) solid line is the theoretical prediction of the SC model with no adjustable parameters. (a) Wavelengths normalized to isolate the dependence of Λ_D^{SC} on D. (b) Wavelength normalized to isolate the dependence of $\Lambda_{\Delta T}^{SC}$ on ΔT.

large outliers at larger values of ΔT.

The last wavelength prediction comes from the TC model and was presented above in Eq. (5.27). The scaled results are shown in Fig. 5.10, with Λ_D^{TC} in Fig. 5.10(a) and $\Lambda_{\Delta T}^{TC}$ in Fig. 5.10(b). Both quantities show strongly linear behavior that is consistent with the theoretical prediction although they tend to overshoot the TC model somewhat.

Based on the wavelength scaling results, the experimental data supports the conclusion that the thermocapillary model is the dominant physical mechanism for this instability. There remains a disagreement between the theoretical prediction of the model and the experimental data, but this can reasonably be attributed to the uncertainty in the material properties, which will be discussed further below, after we examine the growth rate results.

Figure 5.9: Wavelengths normalized by the AP model

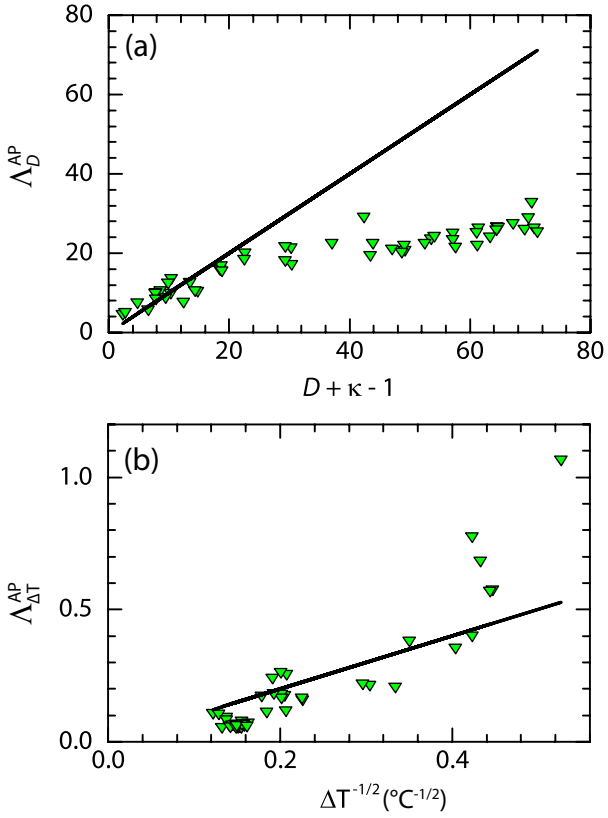

In each case, the (black) solid line is the theoretical prediction of the AP model with no adjustable parameters. (a) Wavelengths normalized to isolate the dependence of Λ_D^{AP} on D. (b) Wavelengths normalized to isolate the dependence of $\Lambda_{\Delta T}^{AP}$ on ΔT.

5.5.4 Nondimensional Growth Rate Comparisons

Beyond scaling the measured wavelengths, we also scaled the growth rates which were measured at the same time. Generally, this section will proceed similarly to the previous one, where we scale the predicted growth rates from each model separately to isolate their dependence on D and ΔT. However, before we treat each model individually, we can probe the consistency of the growth rate and wavelength measurements within the context of general linear stability. Looking at the growth rates for the three models derived in Ch. 2, there is a relationship between the growth rate, b_o, and the wavelength, λ_o, for thin film instabilities which stems from the dispersion relation. Specifically, the nondimensional relationship is

$$\beta_\Lambda \equiv b_o \frac{h_o \mu}{\gamma} = \frac{(2\pi)^4}{3} \Lambda^{-4}, \tag{5.32}$$

where β_Λ is a nondimensional growth rate and $\Lambda \equiv \lambda_o / h_o$ is a nondimensional wavelength. As such, if our growth rate and wavelength measurements exactly

Figure 5.10: Wavelengths normalized by the TC model

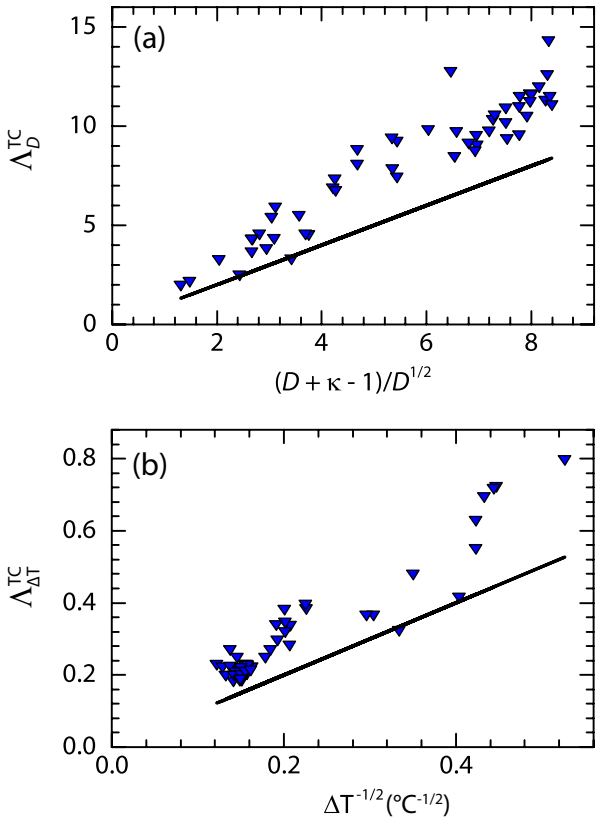

In each case, the (black) solid line is the theoretical prediction of the TC model with no adjustable parameters. (a) Wavelengths normalized to isolate the dependence of of Λ_D^{TC} on D. (b) Wavelengths normalized to isolate the dependence of of $\Lambda_{\Delta T}^{TC}$ on ΔT.

matched the predictions of linear stability analysis applied to thin film instabilities, independent of any specific model, we would expect this relationship to hold. In following our convention from the wavelength scaling, this relationship has been plotted in Fig. 5.11. The solid black line is the prediction from linear stability theory with no adjustable parameters. Generally, there are many points which lie close to the predicted line, but the scatter is large. Due to the large powers involved with making comparisons to the growth rate, even small discrepancies can be magnified quickly. We will discuss this discrepancy further after presenting the results for each individual model in turn. Note that all the scaled growth rates have been plotted on logarithmic axes whereas the scaled wavelengths presented above were plotted on linear axes. This is due to the much larger powers in the scaled growth rates which means that they span a much larger range.

The first growth rate scaling we investigated was for the SC model through Eq. (5.24).

Figure 5.11: Nondimensional growth rate plotted as a function of the nondimensional wavelength

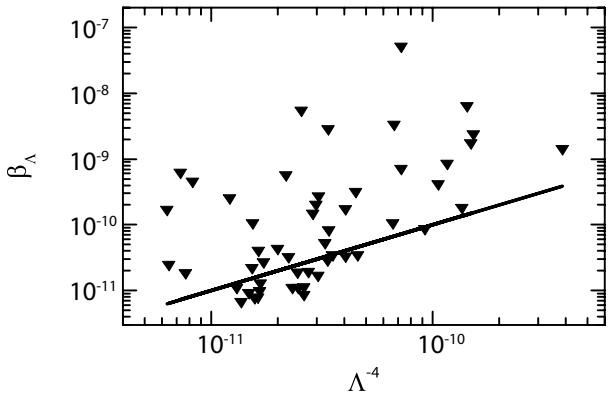

The (black) solid line is the theoretical prediction from linear stability with no adjustable parameters. The nondimensional growth rate is plotted as a function of the nondimensional wavelength.

As with the wavelength scaling, we isolated the functional dependence of the growth rate on D and ΔT. In both Fig. 5.12(a) and (b), the solid line is the theoretical prediction of the SC model with no adjustable parameters. Both of these plots show scatter up to three orders of magnitude.

Next, we isolated the dependencies of Eq. (5.26) to further probe the growth rate predictions of the AP model. Fig. 5.13(a) contains the scaled growth rate β_D^{AP} and Fig. 5.13(b) contains the scaled growth rate $\beta_{\Delta\mathrm{T}}^{\mathrm{AP}}$. The solid lines are the linear stability predictions of the AP model with no adjustable parameters. The data in Fig. 5.13(a) shows a linear relationship with a slight overestimation of the growth. On the other hand, the data in Fig. 5.13(b) is at least 10 orders of magnitude away from the theoretical prediction.

As compared to the AP model, the scaled growth rates of Eq. (5.28) derived from the TC model compare much more favorably. The values of β_D^{TC} plotted in Fig. 5.14(a) show modest agreement with the solid line. The values of $\beta_{\Delta\mathrm{T}}^{\mathrm{TC}}$ plotted in Fig. 5.14(b) show a great deal of scatter.

Due to the stronger dependencies of the growth rate on the key experimental parameters, the scaled growth rates provide a more stringent test of the physical models. Based solely on the scaled growth rate measurements it is more difficult to draw strong conclusions than with the corresponding scaled wavelength data due to the larger scatter. However, the AP model shows a massive disagreement of 10 orders of magnitude with the predictions for the scaled growth rate. Neither the SC nor the TC model predictions show strong agreement with the experimental data, but they

Figure 5.12: Growth rates normalized by the SC model

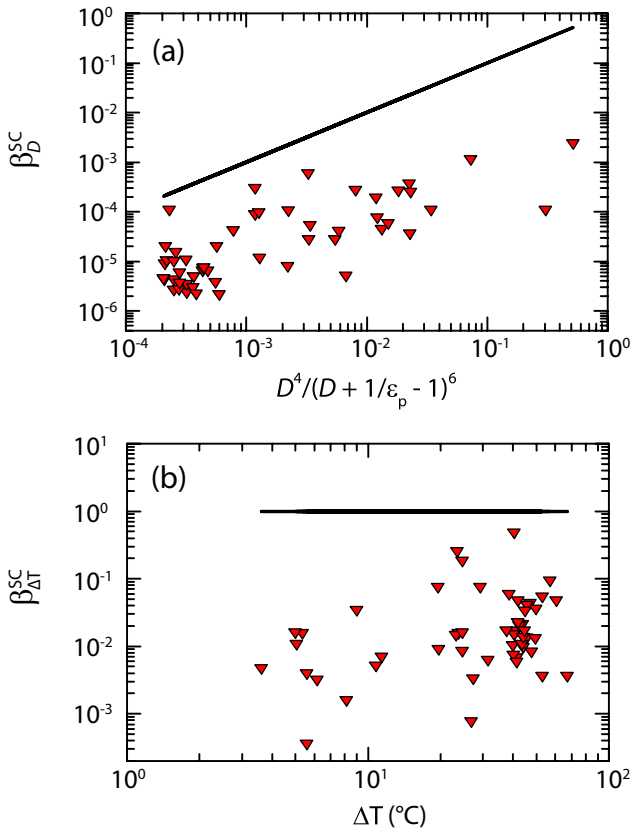

In each case, the (black) solid line is the theoretical prediction of the SC model with no adjustable parameters. (a) Growth rates normalized to isolate the dependence of β_D^{SC} on D. (b) Growth rates normalized to isolate the dependence of $\beta_{\Delta T}^{SC}$ on ΔT.

are significantly better than the AP model.

5.6 Discussion of Redesigned Experimental Setup Results

In this section, we first highlight and summarize the improvements that this chapter has made on previous experimental studies. Then, we comment on some of the remaining experimental challenges which hindered this analysis and could be improved in the future. Finally, we discuss the dominant physical mechanism driving this instability in light of the scaled wavelength and growth rate results presented above.

5.6.1 Comparison to Previous Experimental Studies

As compared to the work of McLeod *et al.* [1], the present study has focused on improving both the experimental setup and the analysis framework. Major

Figure 5.13: Growth rates normalized by the AP model

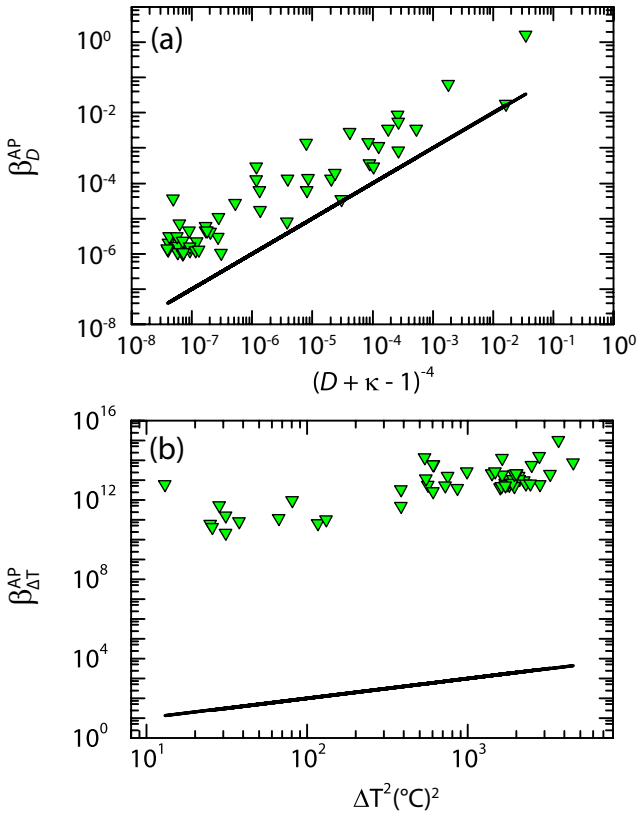

In each case, the (black) solid line is the theoretical prediction of the AP model with no adjustable parameters. (a) Growth rates normalized to isolate the dependence of β_D^{AP} on D. (b) Growth rates normalized to isolate the dependence of $\beta_{\Delta\mathrm{T}}^{\mathrm{AP}}$ on ΔT.

considerations when designing this setup centered around improvements to the thermal stability and improvements to the optical imaging. On the thermal stability front, we used a large integrated aluminum chiller unit for better thermal contact with both the sapphire window and the external circulator. We used an alumina ceramic heater which could access a larger range of temperatures and coupled this with platinum RTDs which were more accurate than thermocouples. This allowed for more precise control of the heater temperature as a function of time. Turning to the optical imaging process, we increased the viewing area so that there was more data for analysis and switched to single wavelength illumination to enhance the contrast of the instability growth. With this improved experimental setup we scanned a much larger range of parameters, both D and ΔT to highlight the differences in the proposed models. We also derived a fitting function for this particular physical system which allowed for the simultaneous extraction of both the wavelength and growth rate of the instability. Finally, we minimized the effects of the thermal

Figure 5.14: Growth rates normalized by the TC model

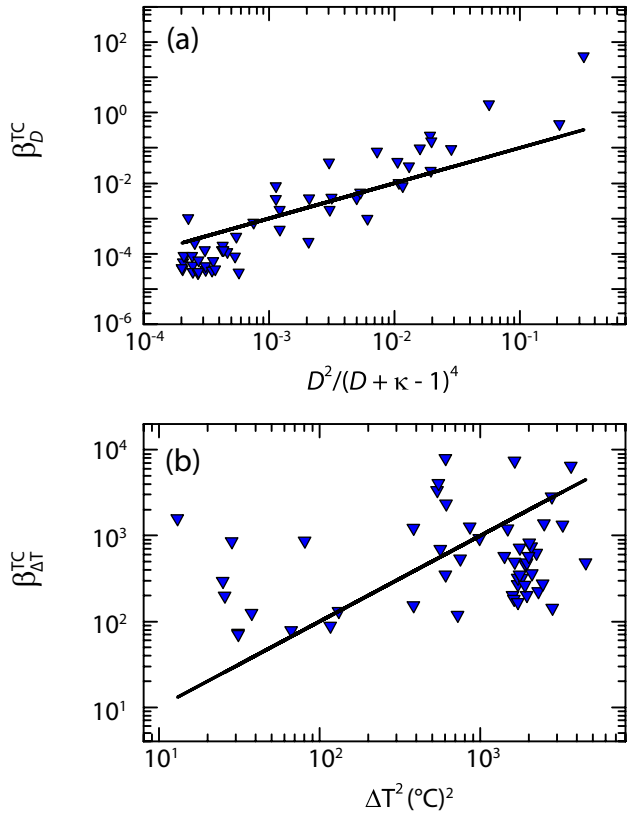

In each case, the (black) solid line is the theoretical prediction of the TC model with no adjustable parameters. (a) Growth rates normalized to isolate the dependence of β_D^{TC} on D. (b) Growth rates normalized to isolate the dependence of $\beta_{\Delta\mathrm{T}}^{\mathrm{TC}}$ on ΔT.

dependence of the material properties by introducing new scalings which account for the variation between experimental runs.

5.6.2 Remaining Experimental Challenges

Even with all the improvements to the experimental setup and the analysis procedure, there were still some areas which could be improved in future studies. First, the amount of thermal paste was not measured or strictly controlled during setup. In hindsight, this is a relatively easy thing to fix and would help reduce the scatter between similar experimental runs. In fact, it would probably be best to remove the thermal paste altogether and use a different heater holder which does not contain an inset. Instead, it could have a polished surface on which the silicon wafer is directly placed. This would eliminate several areas of uncertainty and hopefully improve reproducibility between experimental runs. Next, the larger viewing area can also pose technical difficulties. While it allows for more data collection during an ideal

run, it also imposes a stricter requirement on the cleanliness of the film and the substrates must be level over a larger area to not have interference fringes. Furthermore, the pressure on the spacers was not able to be measured with the experimental setup and could have varied between experimental runs. This uncertainty is further compounded by the fact that the thickness of the silicon wafers was only 279 μm and at this thickness can flex significantly under load. If the silicon was bent by the pressure of the spacers or the specific distribution of the thermal paste then this would have effected both the actual value of D and implicitly the numerically computed value of ΔT. The numerical temperature simulations also are assumed to be cylindrically symmetric, even though most of the components are rectangular. A more accurate, but much more computationally expensive, simulation would do a full 3D simulation of the geometry. At this point, we did not feel like this was the largest source of uncertainty as compared to the thermal paste and so it was not pursued. Additionally, we note that the material parameters of the low molecular weight PS that was used are not well measured, particularly in nanofilms. Whenever possible we have tried to use sources in the literature which specify the molecular weight, but the thermocapillary coefficient in particular is one of the parameters which we could not find as a function of molecular weight. Finally, there is a fundamental difficulty when comparing experimental data to the predictions from linear stability analysis. Since linear stability analysis is predicated upon infinitesimal perturbations, the ideal comparison would be a measurement on an infinitesimal experimental signal. This becomes impractical due to noise, but this analysis has tried to measure the wavelength and growth rate as early as possible. This means that the measured values are inherently noisy and show scatter. Furthermore, the growth rates in particular show large scatter and this is partly due to the way they were measured. The growth rates are computed from the width of a peak in the power spectral density and this value is much harder to estimate than the peak position when the peak is small. This is especially true in the presence of background noise which can obscure the lower edge of the peak at low values of the wavevector. We attribute most of the scatter in the growth rate comparisons to this experimental difficulty.

5.6.3 Dominant Instability Mechanism Indentification

At this point, we are in a position to further discuss which proposed model is best supported by the experimental evidence gathered in this study. Taken as a whole, both the wavelength and the growth rate measurements support the conclusion

that the TC model is consistent with the experimental data and best describes this experimental system. The SC and AP models are inconsistent with the experimental data. For the SC model, this is most clearly shown by the dependence of $\Lambda_{\Delta T}^{SC}$ on ΔT in Fig. 5.8(b). Not only is the data two to three orders of magnitude larger than the theoretical predictions, but it shows a clear dependence on temperature when the SC model would predict no thermal dependence at all. Turning to the AP model, it shows inconsistency in both the wavelength and growth rate data. In Fig. 5.9(a), the experimental wavelength data clearly diverges from the linear theoretical prediction at large values of $D + \kappa - 1$. The disagreement is even worse in Fig. 5.13(b), where the experimental data for $\beta_{\Delta T}^{AP}$ is 10 orders of magnitude larger than the predictions of the AP model.

In comparison to the SC and AP models, the TC model shows the best agreement with the experimental data. Both $\Lambda_{\Delta T}^{TC}$ and Λ_{D}^{TC} show linear behavior consistent with the TC model. The slopes are the same but suggest that there is a systematic discrepancy in one of the material parameters. In a similar manner, the growth rate measurements generally lie close to the model predictions which implies that the model is at least consistent, if not strongly supported, by the data.

Since the data supports the TC mechanism best, we have identified several areas where the SC and AP models do not accurately model the physical system. In the case of the SC model, the underlying physics is predicated upon the presence of surface charge at the interface of the nanofilm. However, there is no clear mechanism for this charge accumulation and it seems that the SC model, while not fundamentally incorrect, does not apply to this physical system. For the AP model, the issues appear to run deeper. Specifically, one of the key assumptions that is made in the derivation is that phonons can propagate coherently through a liquid, even when there is not a well-defined lattice in the molten nanofilm. While the initial experimental investigations of Schäffer *et al.* [4–6] were consistent with the AP model over a small range, the more rigorous investigation in this chapter shows that the AP model is inconsistent with this physical system.

5.7 Summary

In this chapter we have described our experimental investigations into the spontaneous instability which occurs in nanofilms with a free interface subject to a large transverse thermal gradient. Previously in the literature, three mechanisms had been proposed to describe this instability. The SC model is predicated upon the accumu-

lation of surface charge at the interface which destabilizes the free surface of the molten film. The AP model suggests that the instability arises from a destabilizing acoustic radiation pressure which builds up at the interface of the molten film. The TC model hypothesizes that the deformation occurs due to surface tension gradients which arise due to the temperature dependence of the surface tension along the film/air interface.

Using *in situ* optical observations of the instability during the growth process we have measured the characteristic wavelength and growth rate of the instability. We used a new fitting function derived above to fit the power spectral density which allowed for the simultaneous measurement of both of these quantities. When combined with numerical simulations of the temperature in the experimental setup, we compared the experimental data to the predictions of each model. The results of this comparison support the TC model as the dominant physical mechanism and show that the SC and AP models are inconsistent with the experimental data.

Table 5.5: Parameters and thermal conductivities for the thermal simulations

Exp. #	h_o (nm)	d_o (nm)	r_{paste} (mm)	T_{Chill} (°C)	T_{Heat} (°C)	Power (W)	ΔT_{Out} (°C)	ΔT_{sin} (°C)	h_{paste} (mm)	T_H (°C)	ΔT (°C)
1	154	6860	14.1	32.3	150	39.4	118	41.3	426	108	41.3
2	159	3060	20.3	32.9	150	49.0	117	23.7	341	103	23.7
3	159	6870	19.0	32.8	150	47.1	117	53.0	127	130	53.0
4	159	889	22.5	33.0	150	50.2	117	5.27	562	83.5	5.33
5	347	3250	18.0	32.8	120	41.1	87.2	23.2	149	98.0	23.2
6	352	1080	23.1	32.3	120	33.1	87.7	3.43	819	64.8	3.60
7	95.9	6810	18.1	32.9	150	43.7	117	47.3	239	120	47.3
8	96.3	3000	20.5	33.0	150	48.9	117	23.4	347	103	23.4
9	95.9	826	21.5	32.9	150	49.1	117	4.98	611	81.6	5.00
10	157	3060	21.4	42.9	140	47.0	97.1	24.7	149	115	24.7
11	97.5	6810	14.7	42.2	140	37.8	97.8	42.0	176	119	42.0
12	96.4	3000	25.0	42.4	140	40.9	97.6	19.6	344	101	19.6
13	96.7	827	25.0	42.8	140	45.9	97.2	5.05	400	90.9	5.07
14	285	3190	25.0	42.5	140	46.5	97.5	24.7	161	114	24.7
15	287	1020	18.1	42.7	140	46.3	97.3	5.41	375	92.3	5.58
16	155	6870	20.0	23.5	160	47.6	137	49.9	367	115	49.9
17	156	3060	25.0	23.7	160	53.2	136	24.6	472	97.1	24.7
18	96.6	6810	18.0	23.6	160	52.2	136	57.0	199	128	57.0
19	289	3190	22.0	24.2	160	61.3	136	31.4	227	116	31.5
20	300	7010	20.5	24.0	160	58.2	136	67.2	51.5	147	67.2
21	301	7010	22.6	33.2	150	52.2	117	60.5	10.1	144	60.5
22	300	3200	21.5	33.3	150	52.9	117	27.3	220	113	27.4
23	99.6	3000	22.6	24.1	160	59.7	136	29.3	273	111	29.3
24	100	6810	16.9	51.5	130	35.1	78.5	40.5	12.8	126	40.5
25	99.9	3000	19.7	51.8	130	37.6	78.2	19.6	157	109	19.6
26	182	6890	13.0	28.3	155	47.7	127	52.8	207	125	52.8
27	288	4100	18.6	32.7	150	43.5	117	26.8	470	99.1	26.9
28	109	7110	20.0	41.9	150	38.3	108	41.3	330	117	41.3
29	109	7110	19.0	42.2	150	40.8	108	45.6	210	125	45.6
30	143	7140	14.7	41.9	150	37.3	108	40.4	363	115	40.4
31	143	7140	13.0	41.7	150	35.2	108	37.5	479	110	37.5
32	109	7110	19.0	41.7	150	37.4	108	39.9	382	114	39.9
33	115	7120	15.2	32.5	160	41.5	128	43.7	498	112	43.7
34	117	1540	15.8	42.1	150	42.9	108	8.95	604	89.8	8.97
35	97.5	1520	15.2	41.5	150	48.2	108	10.8	398	98.0	10.8
36	158	1360	17.5	41.2	140	43.2	98.8	8.12	448	89.7	8.15
37	97.1	987	18.6	42.2	150	44.8	108	5.57	606	87.8	5.58
38	140	1030	14.1	42.4	150	46.3	108	6.11	510	91.2	6.14
39	101	1520	15.2	33.3	160	52.9	127	11.4	503	93.6	11.4
40	99.5	7100	18.6	41.8	150	39.0	108	42.5	294	119	42.5
41	98.7	7100	13.0	41.7	150	38.2	108	42.0	312	118	42.0
42	123	7120	14.1	41.6	150	37.2	108	40.3	369	115	40.3
43	131	7130	20.5	41.8	150	40.9	108	45.7	212	124	45.7
44	115	7120	14.7	41.8	150	39.7	108	44.2	250	122	44.2
45	123	7120	14.1	32.3	160	41.1	128	43.4	511	111	43.4
46	130	7130	19.0	32.6	160	44.5	127	47.8	356	119	47.8
47	115	7120	14.7	32.6	160	45.2	127	49.5	309	122	49.5
48	149	7150	20.0	41.9	150	39.9	108	44.1	251	122	44.1
49	134	7130	18.5	41.8	150	38.2	108	41.3	333	117	41.3
50	122	7120	18.0	32.4	150	41.1	118	45.0	338	114	45.0
51	145	7150	15.8	32.5	160	42.2	128	44.7	461	114	44.7
52	111	7110	18.6	41.7	150	36.5	108	38.5	436	112	38.5

This table contains the experimental run number, initial film thickness, h_o, and total gap distance, d_o. Next are the experimental values which were used in the simulations: the applied thermal paste radius, r_{paste}, the temperature of the aluminum chiller, T_{Chill}, the temperature of the ceramic heater, T_{Heat}, and the electrical power dissipated in the heater. Finally are the derived values: ΔT_{Out} is the difference between the measured heater and chiller temperatures, ΔT_{sin} is the temperature drop across the sinusoidally deformed bilayer, h_{paste} is the thickness of the thermal paste, T_H is the temperature at the bottom of the polymer film, and ΔT is the temperature drop across the undeformed bilayer.

Table 5.6: Image analysis parameters and measured wavelengths and growth rates

Exp. #	D	Filter (nm)	Image Size (μm×μm)	$k_{\min} \times 10^{-2}$ (1/μm)	t_{final} (min)	t_{meas} (min)	λ_o (μm)	$b_o \times 10^{-4}$ (1/s)
1	44.6	633	498 × 500	5.03	153.75	95.75	69.0	1.28
2	19.3	633	893 × 1190	5.03	66.75	26.75	67.4	10.4
3	43.2	633	397 × 377	3.14	174.75	34.75	78.6	2.93
4	5.59	633	558 × 686	5.03	36.75	14.75	70.7	27.1
5	9.36	488	891 × 1190	3.14	69.00	13.00	100.2	74.8
6	3.08	488	892 × 1190	2.51	480.00	71.00	120.6	3.38
7	71.0	488	696 × 901	5.03	110.00	34.00	57.6	4.21
8	31.1	488	432 × 598	5.03	108.00	16.00	44.5	35.1
9	8.61	515	516 × 870	5.03	135.25	36.25	58.4	3.93
10	19.5	633	886 × 1190	5.03	81.75	15.75	67.6	14.7
11	69.8	488	610 × 874	5.03	157.00	28.00	49.3	4.73
12	31.1	488	730 × 979	5.03	92.00	18.00	60.8	9.03
13	8.55	488	774 × 1200	5.03	61.00	14.00	57.0	9.52
14	11.2	515	884 × 644	3.14	48.25	13.25	99.7	166
15	3.55	532	895 × 691	5.03	104.50	20.50	82.0	14.0
16	44.2	633	898 × 911	5.03	98.75	19.75	54.4	10.6
17	19.6	532	888 × 1190	5.03	21.75	8.75	64.6	69.7
18	70.5	488	515 × 569	5.03	70.00	13.00	45.7	15.6
19	11.0	532	613 × 1200	5.03	15.75	8.75	65.3	76.9
20	23.4	532	569 × 1190	3.14	23.50	6.50	87.8	45.5
21	23.3	532	745 × 645	3.14	22.50	6.50	85.5	533
22	10.7	532	887 × 1190	3.14	43.50	6.50	91.2	36.6
23	30.1	515	826 × 1190	5.03	18.25	6.25	42.6	24.6
24	67.9	515	394 × 858	5.03	152.25	40.25	53.7	77.5
25	30.0	515	850 × 1120	5.03	152.25	57.25	62.7	2.69
26	37.9	488	815 × 1200	5.03	47.00	14.00	70.3	49.2
27	14.2	515	590 × 969	3.14	162.25	139.25	93.0	1.39
28	65.2	488	587 × 886	5.03	137.00	81.00	57.3	1.84
29	65.5	488	823 × 642	5.03	174.00	21.00	53.3	6.90
30	50.0	515	382 × 578	5.03	162.75	93.75	59.3	3.16
31	49.8	532	433 × 1020	5.03	400.75	163.75	65.8	2.53
32	65.2	488	765 × 519	5.03	434.00	137.00	56.7	0.907
33	61.9	488	474 × 1200	5.03	403.00	140.00	48.9	1.84
34	13.2	515	213 × 213	5.03	323.25	89.25	40.0	11.2
35	15.6	515	264 × 267	5.03	118.50	63.50	40.7	2.32
36	8.58	633	510 × 583	5.03	359.75	101.75	62.8	1.98
37	10.2	488	394 × 596	5.03	329.00	206.00	49.0	1.55
38	7.35	515	284 × 355	5.03	74.75	24.75	43.6	6.16
39	15.1	488	465 × 617	5.03	151.75	41.75	41.8	2.31
40	71.4	488	463 × 766	5.03	233.00	97.00	50.7	1.95
41	71.9	488	774 × 1190	5.03	279.00	71.00	48.9	1.96
42	57.9	532	885 × 1190	5.03	370.75	162.75	61.8	0.959
43	54.3	488	858 × 812	5.03	192.75	51.75	57.3	4.04
44	62.1	488	894 × 875	5.03	241.00	106.00	57.0	1.65
45	57.9	532	893 × 857	5.03	434.50	134.50	55.9	1.10
46	54.8	532	887 × 664	5.03	189.75	69.75	57.4	1.83
47	61.8	532	510 × 469	5.03	187.50	57.50	51.6	2.33
48	47.9	633	882 × 912	5.03	188.75	50.75	59.2	5.17
49	53.2	532	735 × 1200	5.03	425.75	97.75	59.2	1.15
50	58.3	633	712 × 1200	5.03	371.75	130.75	50.1	3.97
51	49.4	633	786 × 1100	5.03	442.75	93.75	55.5	3.34
52	64.1	532	694 × 945	5.03	495.75	228.75	55.2	4.61

This table contains the experimental run number and normalized gap separation distance, $D = d_o/h_o$. Next are the auxiliary experimental information which was used during the analysis process: the wavelength of the optical filter chosen, the size of the subimage which was selected for analysis (H×W), the lower bound of the bandpass filter, $k_{\min}$, and the point in the time series at which the analysis process was terminated, t_{final}. Finally are the results of the analysis procedure: the time of measurement, t_{meas}, the measured wavelength, λ_o, and the measured growth rate, b_o.

Table 5.7: Material properties at the temperature of each experimental run

Exp. #	D	k_a mW/m-°C	$\kappa \equiv k_a/k_p$	γ (mN/m)	μ (Pa*s)	$C^{\mathrm{SC}} \times 10^3$ $\left(\sqrt{\mu\mathrm{m}}\right)$	C^{AP} $\left(\sqrt{°\mathrm{C}}\right)$	C^{TC} $\left(\sqrt{°\mathrm{C}}\right)$
1	44.6	31.9	0.249	32.4	16.1	8.32	128	296
2	19.3	31.6	0.247	32.8	28.0	8.37	129	300
3	43.2	33.4	0.260	30.7	4.36	8.10	123	283
4	5.59	30.2	0.244	34.3	223	8.57	135	308
5	9.36	31.2	0.245	33.2	42.5	8.43	131	303
6	3.08	28.9	0.242	35.8	8030	8.75	141	316
7	71.0	32.7	0.255	31.5	7.52	8.20	125	289
8	31.1	31.6	0.246	32.8	28.6	8.38	130	300
9	8.61	30.1	0.244	34.4	295	8.58	136	309
10	19.5	32.4	0.252	31.8	10.6	8.25	126	292
11	69.8	32.7	0.254	31.5	7.74	8.21	125	289
12	31.1	31.4	0.245	32.9	33.0	8.40	130	301
13	8.55	30.8	0.244	33.7	85.8	8.49	133	305
14	11.2	32.3	0.252	31.9	11.8	8.27	127	293
15	3.55	30.8	0.245	33.6	76.1	8.48	133	305
16	44.2	32.4	0.253	31.8	10.5	8.25	126	292
17	19.6	31.2	0.245	33.2	45.3	8.43	131	303
18	70.5	33.3	0.259	30.8	4.59	8.12	123	283
19	11.0	32.4	0.253	31.8	10.4	8.25	126	292
20	23.4	34.5	0.267	29.3	2.03	7.92	119	272
21	23.3	34.3	0.266	29.5	2.29	7.95	120	274
22	10.7	32.2	0.251	32.0	12.9	8.28	127	294
23	30.1	32.1	0.251	32.1	13.9	8.29	127	294
24	67.9	33.1	0.258	30.9	5.28	8.14	124	285
25	30.0	32.0	0.250	32.3	15.3	8.31	128	295
26	37.9	33.1	0.257	31.1	5.74	8.15	124	286
27	14.2	31.3	0.245	33.1	37.1	8.42	131	302
28	65.2	32.5	0.253	31.7	9.10	8.23	126	291
29	65.5	33.0	0.257	31.1	5.82	8.15	124	286
30	50.0	32.4	0.253	31.8	10.5	8.25	126	292
31	49.9	32.0	0.250	32.2	14.8	8.30	128	295
32	65.2	32.3	0.252	31.9	11.3	8.26	127	292
33	61.9	32.2	0.251	32.1	13.1	8.28	127	294
34	13.2	30.7	0.244	33.8	95.9	8.50	133	306
35	15.6	31.2	0.245	33.2	40.2	8.42	131	302
36	8.58	30.7	0.244	33.8	97.5	8.51	133	306
37	10.2	30.5	0.244	34.0	124	8.52	134	306
38	7.35	30.8	0.244	33.7	83.5	8.49	133	305
39	15.1	30.9	0.245	33.5	61.3	8.47	132	304
40	71.4	32.7	0.254	31.5	7.82	8.21	126	289
41	71.9	32.6	0.254	31.6	8.38	8.22	126	290
42	57.9	32.4	0.252	31.8	10.9	8.26	127	292
43	54.3	33.0	0.257	31.1	5.91	8.16	124	286
44	62.1	32.8	0.256	31.3	6.85	8.18	125	288
45	57.9	32.1	0.251	32.1	13.7	8.29	127	294
46	54.9	32.7	0.255	31.5	7.66	8.21	125	289
47	61.8	32.9	0.256	31.3	6.65	8.18	125	287
48	47.9	32.8	0.256	31.3	6.87	8.19	125	288
49	53.2	32.5	0.253	31.7	9.25	8.24	126	291
50	58.9	32.3	0.252	31.9	11.8	8.27	127	293
51	49.4	32.3	0.252	31.9	11.7	8.27	127	293
52	64.1	32.2	0.251	32.1	13.3	8.29	127	294

This table contains the experimental run number and the normalized gap separation distance, $D = d_o/h_o$. Next are the material parameters evaluated at the temperature of the PS-air interface for each experimental run: the thermal conductivity of the air, k_a, the thermal conductivity ratio, κ, the surface tension, γ, and the viscosity, μ. Finally are the quantities which scale the nondimensional wavelengths and growth rates in Table 5.4: C^{SC}, C^{AP}, and C^{TC}.